The Pennsylvania State University

The Graduate School

Department of Mechanical and Nuclear Engineering

DEVELOPMENT OF HIGH-ENERGY CATHODE MATERIALS

FOR LITHIUM-SULFUR BATTERIES

A Dissertation in

Mechanical Engineering

by

Tianren Xu

Submitted in Partial Fulfillment
of the Requirements
for the Degree of

Doctor of Philosophy

December 2013

The dissertation of Tianren Xu was reviewed and approved* by the following:

Donghai Wang
Assistant Professor of Mechanical Engineering
Dissertation Advisor, Chair of Committee

Chris D. Rahn
Professor of Mechanical Engineering

Adri van Duin
Associate Professor of Mechanical Engineering

Qing Wang
Professor of Materials Science and Engineering

Karen A. Thole
Professor of Mechanical Engineering
Head of the Department of Mechanical and Nuclear Engineering

*Signatures are on file in the Graduate School

ABSTRACT

Rechargeable lithium-sulfur batteries are energy storage devices based on the reversible electrochemical reaction between lithium metal and elemental sulfur. When fully utilized, its energy density could reach 3-5 times that of currently marketed lithium ion batteries. This thesis describes the work focused on the development of cathode materials for high-energy lithium-sulfur batteries. More specifically, the design, synthesis, and characterization of cathode materials based on porous carbon-sulfur (C-S) composites are discussed.

The work described in Chapter 2 focused on tuning the pore structure of porous carbon in order to improve electrochemical performance of the C-S composite cathode material. It was found the pore volume of the porous carbon directly affect the practical energy output of the composite, as it limits the useful sulfur content in the composite. Meanwhile, the pore sizes of the porous carbon need to be restrained for desirable sizes of sulfur particles in the composites for satisfactory battery performance. These two parameters are competing and need to be balanced. The proposed porous carbon, HPC, affords a high pore volume with pore sizes restrained under 20nm. This carbon material can embed up to 80wt.% sulfur in its pore structure and still lead to exceptional battery performance.

The work described in Chapter 3 focused on forming secondary structure of C-S composite in order to improve its energy density (both gravimetric and volumetric). Besides the nano-structure, the exterior morphology of C-S composite particles is also critical for its battery performance as the cathode material. Syntheses focused on the nano-structuring without proper control of particle morphology normally result in particles too small for battery applications, plaguing battery fabrication and failing to reach the full potential of the electrode materials. This work took on the challenge to control multi-scale features in C-S composite. The proposed PSC porous carbon spheres not only have a high volume of nano-sized pores, but also exhibit desirable

particle-size distribution for battery applications. The resultant C-S composite showed enhanced battery performance on various aspects, including tap density, areal capacity, and projected gravimetric and volumetric energy density of the whole battery. The proposed synthesis method is also highly scalable and versatile to incorporate extra building blocks into the C-S composite.

The work described in chapter 4 focused on functionalizing porous carbon to stabilize battery performance. Lithium-sulfur batteries severely suffer from performance decay because sulfur has diffusion loss in forms of lithium polysulfides. It was observed that nitrogen doping in carbon could significantly enhance carbon's adsorption of polysulfides, consequently mitigate the diffusion loss of polysulfides and performance decay. This work details the synthesis and characterization of nitrogen-doped porous carbon, the study of its enhanced interaction with sulfur and polysulfides, and improved battery performance from its sulfur composite.

TABLE OF CONTENTS

LIST OF FIGURES

LIST OF TABLES

ACKNOWLEDGEMENTS

To my beautiful wife, Lili, and my pride and joy, Max

Chapter 1

Introduction to the development of lithium-sulfur batteries

1.1 Introduction to Li-S batteries

The last two decades saw tremendous advancement of rechargeable battery technology and their expansion in diverse applications. Several generations of rechargeable batteries based on different chemistries have been developed and enabled various endeavors of human kind. For instance, battery-powered portable electronics have allowed portable workplaces and greatly enhanced work efficiency. They provide accessible information and computing capacity everywhere we go, whether in commute or at the dentists' waiting room. In addition, rechargeable batteries are prominent options as energy storage devices that are offering solutions to the grim environmental challenges in front of us. They are a necessary component to harvest green energies like solar and wind, by offering storage solution and leveling off the volatile fluctuation associated with these energy forms. They are also due to replace gasoline as the power source for automobiles, slashing greenhouse emission on the roads.

Lithium-based batteries are the most promising candidates among all batteries chemistries, because of their high energy density, long cycle life, and relatively low cost. In particular, lithium-ion batteries, based on intercalation mechanism in metal oxide cathodes and graphite anodes, are predominant on the current market. This technology was commercialized by

Sony in 1991 and has received extensive development by industry and research institutes around the globe. The state-of-the-art lithium-ion batteries can reach an energy density of ~200 Wh/Kg, representing the best performance among all commercialized batteries. However, this value is closely approaching the limit of the battery chemistry.

Li-S batteries use lithium metal as the anode and sulfur as the cathode. The complete reaction to form Li_2S generates a capacity of 1672 mAh/g and a specific energy of 2600 Wh/Kg. The projected specific energy of whole Li-S battery cells can reach 3-5 times that of lithium ion batteries. Should these battery cells replace current lithium ion batteries on the market, it roughly can be interpreted as one-week use of smartphones, two-days use of laptop, 300 miles driving of electric vehicles, before any of these devices has to get charged. Today, as the technology of lithium ion batteries is approaching its limit, new chemistries of rechargeable battery such as Li-S batteries are high needed to sustain the quick expansion our electrified society. Indeed, research enthusiasm on this topic is quickly accumulating these years, indicated by the number of publications shown in **Figure 1-1**. As a result, demonstrated battery performance has thoroughly advanced, so is our understanding on this technology.

Research on Li-S batteries started in the late 60's and cooled down with the advent and commercialization of lithium ion batteries. The apparent advantages of Li-S batteries include: its high energy density, next only to the remote Li-air batteries; abundance of sulfur in the nature and its low cost; low toxicity; among others. Although not yet commercialized, Li-S batteries are under development by many companies and research institutes. Notable companies include Sion Power Inc., which has been a leader for this technology. Their Li-S batteries powered the QinetiQ Zephyr to set the world record for the longest duration by unmanned flight in 2010, which benefited from the lightweight and high energy density of Li-S batteries. Another superiority of

Li-S batteries is its tolerance on ambient temperature. They were reported to be maintaining

battery performance at a reasonably high level at -30ºC. This trait makes Li-S batteries attractive

to military and even aerospace applications.[1]
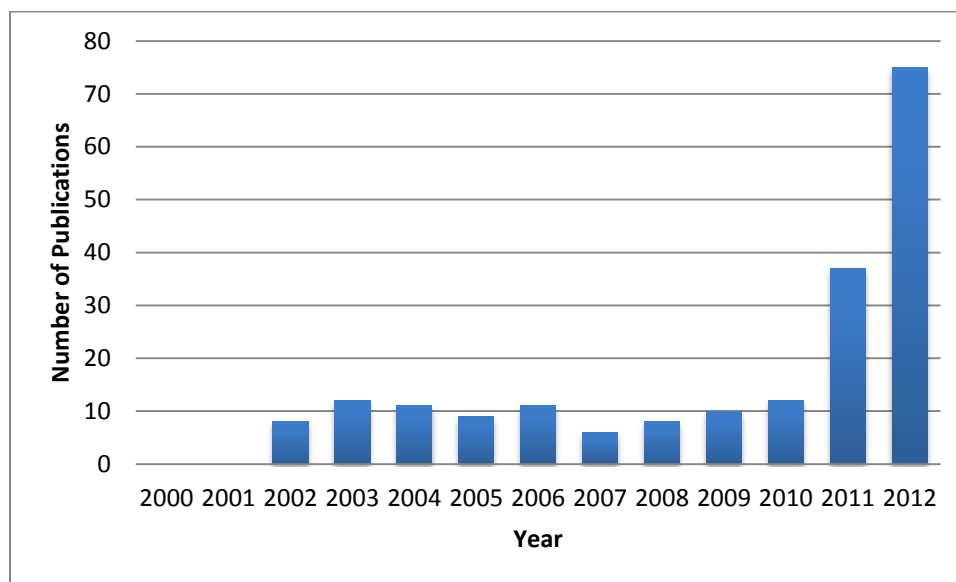
Figure 1-1. Number of publications on Li-S batteries.

1.2 Operation mechanism of Li-S batteries

Li-S batteries operate by a multi-step reaction between sulfur (S_8) and lithium. Lithium polysulfides (i.e., Li_2S_x, $8 \geq x \geq 3$), lithium disulfide (Li_2S_2), and finally lithium sulfide (Li_2S) are formed in sequence during discharge (the lithiation process), with the reverse occurring during charge (the delithiation process). Energy converts between its chemical and electrical forms as the S-S bonds break and re-form. In the most common configuration, sulfur is mixed with conductive carbon and binder to form the cathode; while lithium metal is used as the anode. A polymer membrane soaked with organic liquid electrolyte is used to separate the cathode and anode. Ions conduct through the liquid electrolyte while electrons conduct through the outer circuit. Similar to conventional Li-ion batteries based on intercalation chemistry, lithium ions (Li^+) shuttle between the cathode and anode during battery cycling. During discharge, lithium ions transport to the cathode, break the S-S bonds, and form Li_2S as the final product. During charge, Li_2S is oxidized to elemental S, as lithium ions transport back to the anode and deposit on the anode. While the chemistry for the lithium anode is a relatively straightforward process of metal plating/striping, it is more complicated on the sulfur cathode (**Figure 1-2**). Sulfur converts through multiple phases of polysulfides before it gets completely reduced to Li_2S during discharge; Li2S is then oxidized in the reverse way back to sulfur during charge. Reaction intermediates, lithium polysulfides (i.e., Li_2S_x, $8 \geq x \geq 3$), are soluble in the organic liquid electrolyte. In contrast, lithium disulfide (Li_2S_2) and lithium sulfide (Li_2S) are insoluble and would precipitate out of the electrolyte solution once formed. For the complete conversion from S to Li_2S, this reaction releases an energy density of 2600 Wh kg^{-1} and a specific capacity of 1672 mAh g^{-1}, calculated based on the mass of sulfur.
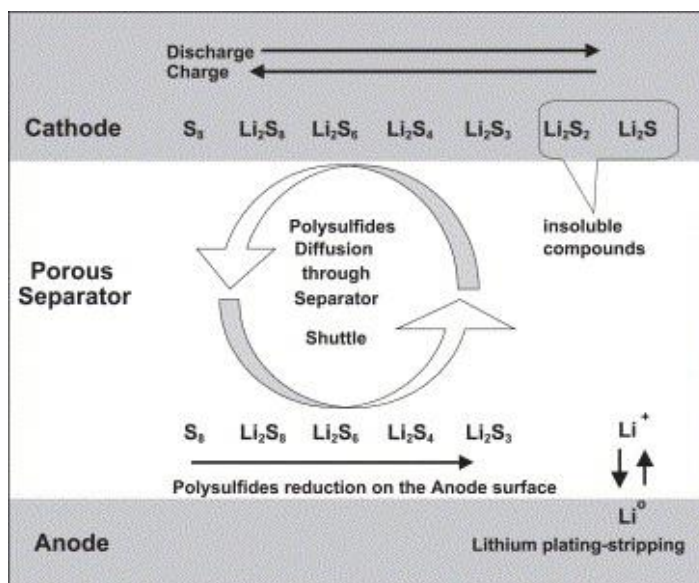
Figure 1-2. Electrochemical reactions of Li-S batteries.[2]
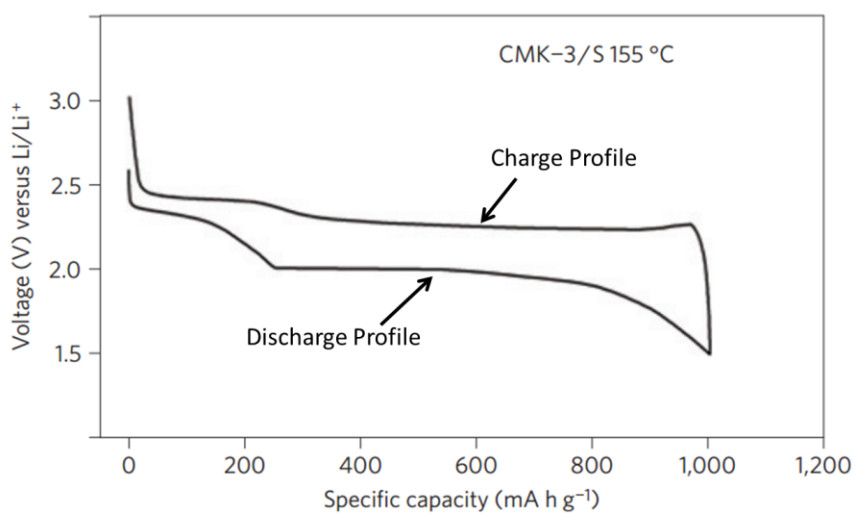
Figure 1-3. Galvanostatic discharge–charge profiles of the first cycles of the carbon–sulfur composites.[3]

Figure 1-3 shows a typical charge/discharge profile of Li-S batteries tested at room temperature, repeated by various publications. The discharge profile exhibits two plateaus, the first at ~2.3V and the second at ~2.1V. Each plateau in the profiles corresponds to one

electrochemical redox reaction (or possibly multiple simultaneous reactions in Li-S batteries where multiple reactive species co-exist) in the battery system. Many researchers believe that the higher plateau at ~2.3V corresponds to the formation of long-chained polysulfides (Li2S$_n$, n≥6), starting with the S_8 ring cut open by Li^+ ions; and that the lower plateau at ~2.1V corresponds to the long sulfur-chains getting further broken down to shorter chains (Li2S$_n$, 2<n<6) and ultimately to Li_2S_2 and Li_2S. Note that the total capacity is significantly lower than the theoretical value of 1680 mAh/g, a challenge that researchers have yet to address. The charge profile also exhibits two plateaus but at higher potentials (~2.3C and ~2.4V, respectively), which may not be distinctive and sometimes merge into one big slope. These plateaus in the charge profile should correspond to the reaction in reverse process of the discharge reactions. In-situ XRD study clearly showed the vanishing of sulfur signals from the cathode and emergence of Li_2S signals during of discharge.[4] During charging, Li_2S signals gradually disappeared and S signals returned. This study well confirmed the conversion of S to Li_2S and the reversibility of this reaction. The formation and evolution of polysulfides as reaction intermediates were well characterized by UV-vis spectroscopy and high performance liquid chromatography (HPLC).[5,6] These studies confirmed the formation of various polysulfides (i.e., Li_2S_x, 8≥x≥3) and their dissolution in the electrolyte during battery cycling. However, the complex composition and behavior of polysulfides are only partly understood. For example, the composition of polysulfides also includes radical forms, such as S3•$^-$. Polysulfides are also known to disproportionate in the electrolyte, illustrated in **Figure 1-4**. Species would split or combine to change the length of their sulfur chain and form equilibriums. The complex system of polysulfides and their disproportionation behavior make it difficult to isolate, identify, and characterize single species of polysulfides in the electrolyte.

$$2S_n{}^{2-} \longleftrightarrow S_m{}^{2-} + \frac{n-m}{8}S_8$$

$$2S_n{}^{2-} \longleftrightarrow S_{n+m}{}^{2-} + S_{n-m}{}^{2-}$$

$$S_n{}^{2-} \longleftrightarrow 2S_{n/2}{}^{\bullet\,-}$$
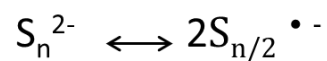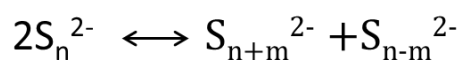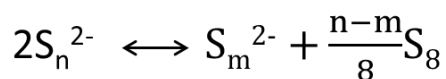
Figure 1-4. Examples of equilibriums between various polysulfide species existing in the electrolyte of Li-S batteries.
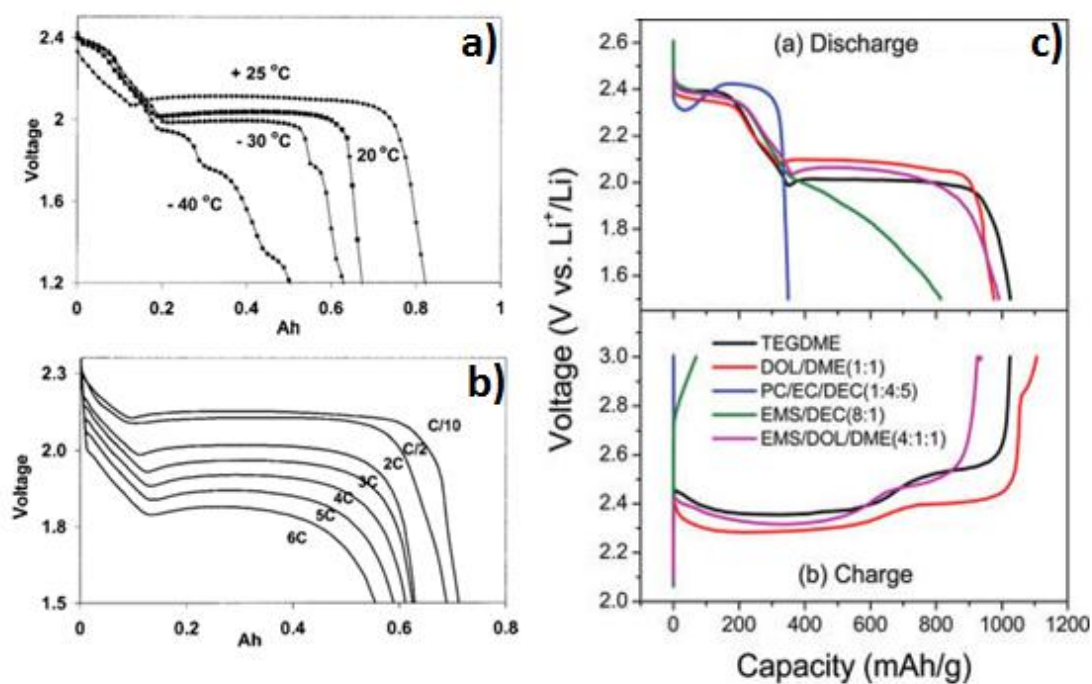
Figure 1-5. a) temperature dependence of discharge profile; b)current rate dependence of discharge profile; c)electrolyte dependence of charge/discharge profile[1,7]

The charge/discharge profile of Li-S batteries is sensitive to many factors of the testing conditions (Figure 1-5). Current rate and testing temperature can affect the charge/discharge profile of Li-S batteries, as they can to Li-ion batteries, due to limit on reaction kinetics.[1] In the particular case of Li-S batteries, testing temperature and electrolyte composition may also affect the profile by affecting the polysulfide transport property of electrolyte.[7]

Major challenges exist to fully realize the theoretical capacity of 1672 mAh g^{-1} for Li-S batteries. In addition, the battery cycle life is short, plagued by severe capacity decay. As a result, Li-S batteries currently cannot surpass Li-ion batteries in energy density and are not ready to replace Li-ion batteries on the market. The mechanism for low attainable energy and fast decay are still under debate but are usually attributed to the following.

Firstly, kinetics of reactions involving solid-state sulfur species, namely S, Li_2S_2, and Li_2S, are slow due to their low conductivity. For instance, the electrical conductivity of sulfur at room temperature is $\sim 10^{-17}$ S/cm, compared with $\sim 10^{-5}$ for common cathode materials of lithium ion batteries.[8] A good contact with a conductive network and well confinement of particle growth is essential for sulfur to react and reach a high capacity. Early reports often use a simple grinding mixture of sulfur and conductive carbon (commonly, acetylene black or Super P) as the cathode materials.[9–11] The resulting capacity is mostly under half of the theoretical value, or 836 mAh/g, likely due to large particles of inactive sulfur particles and their loose connection with the conductive network. A large portion of publications on Li-S batteries focused on novel designs of sulfur nano-composites as cathode materials and significantly increased the achieved capacity.

Secondly, polysulfides would dissolve in the organic solvent. As unavoidable reaction intermediates, polysulfides (i.e., Li_2S_x, $8 \geq x \geq 3$), are soluble in electrolyte. The dissolved

polysulfides would diffuse in the battery, driven by concentration gradient (Fick's law). This property of polysulfides causes a series of problems. 1) When polysulfides diffuse and stay out of the conductive network of the cathode, they become inactive for electrochemical reactions. As a result, the discharge reaction is incomplete and achieved capacity is (significantly) lower than the theoretical value. Both in-situ and ex-situ observation showed the existence of polysulfides in electrolyte throughout a battery cycle, although their concentration may depend on the cathode material.[5,12] 2) Dissolved polysulfides would lose electrons to the lithium anode and retrieve electrons on the cathode while diffusing between electrodes, causing an internal short-circuit. This behavior is termed polysulfide shuttle effect, which not only suppresses charge efficiency at a low level, but also causes safety concerns due to severe heat generation.

1.3 Development of cathode materials for Li-S batteries

Development of sulfur-containing cathode material has been the focus of research on Li-S batteries. As previously introduced, mediocre performance of Li-S batteries is attributed to two properties related to sulfur: its low electrical conductivity and diffusion loss of its lithiated products, polysulfides. Naturally, majority of researches are conducted on where these problems start, or the cathode. Common proposals to improve battery performance include: 1. Constrain particle size of sulfur on nano-size to achieve facile electron conduction in short pathways; 2. Closely hybridize sulfur with conductive network, also for facile electron conduction; 3. Adsorb the dissolved polysulfides to mitigate diffusion loss and performance decay. Among all the works done on this topic, the following concepts attracted the substantial attention and were studied by many research groups around the globe: porous carbon-sulfur composites, fullerene carbon-sulfur composites, and conductive polymer-sulfur composites.

1.3.1 porous carbon-sulfur composites

Porous carbon materials are widely used form sulfur-composites and used as cathode materials for Li-S batteries. The synthesis of these composites harnesses the low melting point of sulfur (115°C). By heating sulfur beyond its melting point in a mixture with porous carbon, capillary force would drive the molten sulfur into the pores of carbon with even distribution. Well-designed porous carbon frameworks can confine sulfur particles at the nanoscale, serving to address both of the core challenges of Li-S batteries. Such frameworks provide a highly-conducting network for electron transfer, thus enabling faster lithiation/delithiation process and

improving sulfur utilization. In addition, their high surface area can trap polysulfides in the cathode through physical adsorption and thus improve capacity retention during cycling. An ideal carbon framework for this application should have the following criteria: (i) high electrical conductivity; (ii) a high pore volume to allow more sulfur in the composite; (iii) a large surface area to afford more electrochemical reaction sites, as well as stronger adsorption of polysulfides; and (iv) a mechanically stable framework to sustain the volume changes of the active materials during electrochemical reactions.

Tremendous work has been done searching for the optimal pore structure of carbon framework. Nazar et al. pioneered such composites by using mesoporous carbon CMK-3 as the conductive framework for sulfur.[3] Sulfur was confined in the mesopores (3-4 nm channel voids), resulting in a high utilization rate (i.e. a specific high capacity). At the same time, the high surface area of CMK-3 promoted polysulfides adsorption and improved cycle stability. Capacity up to 1,320 mAh/g was attained.
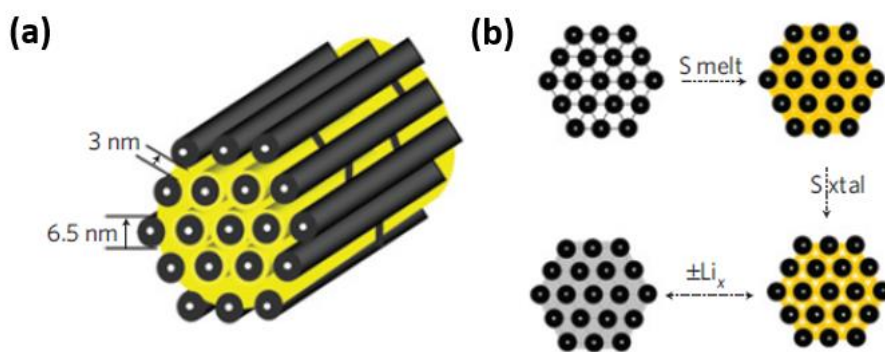
Figure 1-6. (a) A schematic diagram of the sulphur (yellow) confined in the interconnected pore structure of mesoporous carbon (CMK-3). (b) Schematic diagram of composite synthesis by impregnation of molten sulphur, followed by its densification on crystallization. The lower diagram represents subsequent discharging–charging with Li, illustrating the strategy of pore-filling to tune for volume expansion/contraction.[3]

Later, Liang et al. reported a hierarchically structured sulfur-carbon (S/C) nanocomposite material as the high surface-area cathode for rechargeable lithium batteries.[13] A porous carbon with a uniform distribution of mesopores of 7.3 nm has been synthesized through a soft-template synthesis method. The potassium hydroxide activation of this mesoporous carbon results in a bimodal porous carbon with added microporosity of less than 2 nm to the existing mesopores without deterioration of the integrity of the original mesoporous carbon. Elemental sulfur has been loaded to the micropores through a solution infiltration method. The resulted S/C composites with various loading level of sulfur have a high surface areas and large internal porosities. These materials have been tested as novel cathodes for Li/S batteries. The results show that the cyclability and the utilization of sulfur in the Li/S batteries have been significantly improved. The large internal porosity and surface area of the micro-mesoporous carbon is essential for the high utilization of sulfur. A hierarchical meso/microporous carbon matrix was also employed, resulting in high initial capacity.
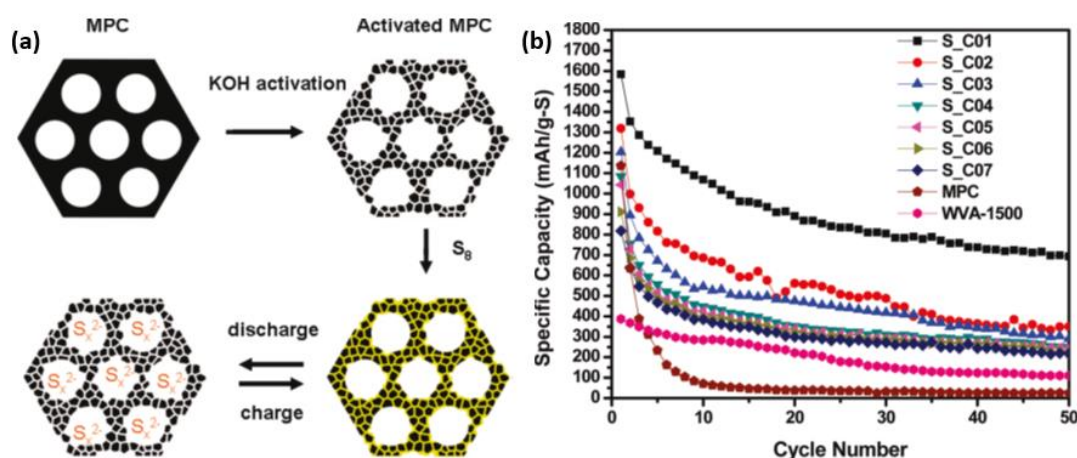
Figure 1-7. (a) Illustration of the S/C composite cathode material by using a bimodal porous carbon as the support (b) Specific discharge capacity of S/C composites.[13]

Recently, Guo et al. explored to permanently retained sulfur in the porous carbon framework in forms of metastable sulfur allotropes of S_{2-4}.[14] The pores of the carbon framework were creased so small that only smaller sulfur allotropes can penetrate while S_8 can't. The confined S_{2-4} as a new cathode material demonstrated an altered electrochemical behavior and can totally avoid the unfavorable dissolution of polysulfides, if they ever existed in this system. Li−S batteries based on this concept exhibit unprecedented electrochemical behavior with high specific capacity, good cycling stability, and superior rate capability, which promise a practicable battery with high energy density for applications in portable electronics, electric vehicles, and large-scale energy storage systems.
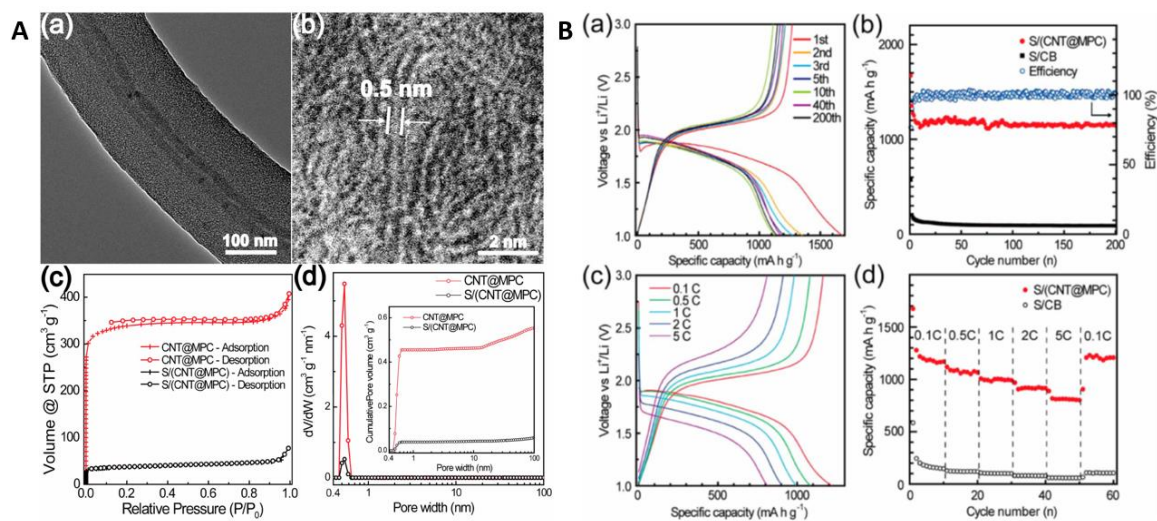
Figure 1-8. Structural characterizations of CNT@MPC. (a) TEM image of a CNT@MPC nanocable. (b) ABF-STEM image showing the carbon channels in the coating layer, in which dark gray part represents the carbon wall, while light gray represents the carbon channel. (c) N_2 adsorption/desorption isotherms and (d) pore size distribution plots of the CNT@MPC and S/(CNT@MPC); (insets: cumulative pore volume). B. Electrochemical properties in carbonate-based electrolyte. (a) GDC voltage profiles of S/(CNT@MPC) at 0.1 C. (b) Cycling performance of S/(CNT@MPC) and S/CB at 0.1 C (blue circles show the Coulombic efficiency of S/(CNT@MPC)). (c) GDC voltage profiles of S/(CNT@MPC) at different discharge/charge rates. (d) Rate capabilities of S/(CNT@MPC) and S/CB.[14]

Encapsulating sulfur in hollow carbon capsules is another good approach.[15] The interior void space, porous shell structure, chemical make-up of the shell, and the methodology used to infuse sulfur into the capsules are designed with four specific aims in mind: 1) maximize the amount of sulfur sequestered by the capsules; 2) minimize lithium polysulfide dissolution and shuttling in the electrolyte; 3) preserve fast transport of lithium ions to the sequestered sulfur by ensuring good electrolyte penetration; and 4) facilitate good transport of electrons from the poorly conducting sulfur. Used as the cathode material in Li–S secondary batteries, the as-prepared C@S carbon–sulfur nanocomposite capsules are found to manifest promising electrochemical behavior upon extended cycling for 100 cycles at 850 mA/g (0.5 C), consistent with our goals in designing the capsules. The electrochemical stability of the C@S composites is confirmed using extended scan cyclic voltammetry measurements.
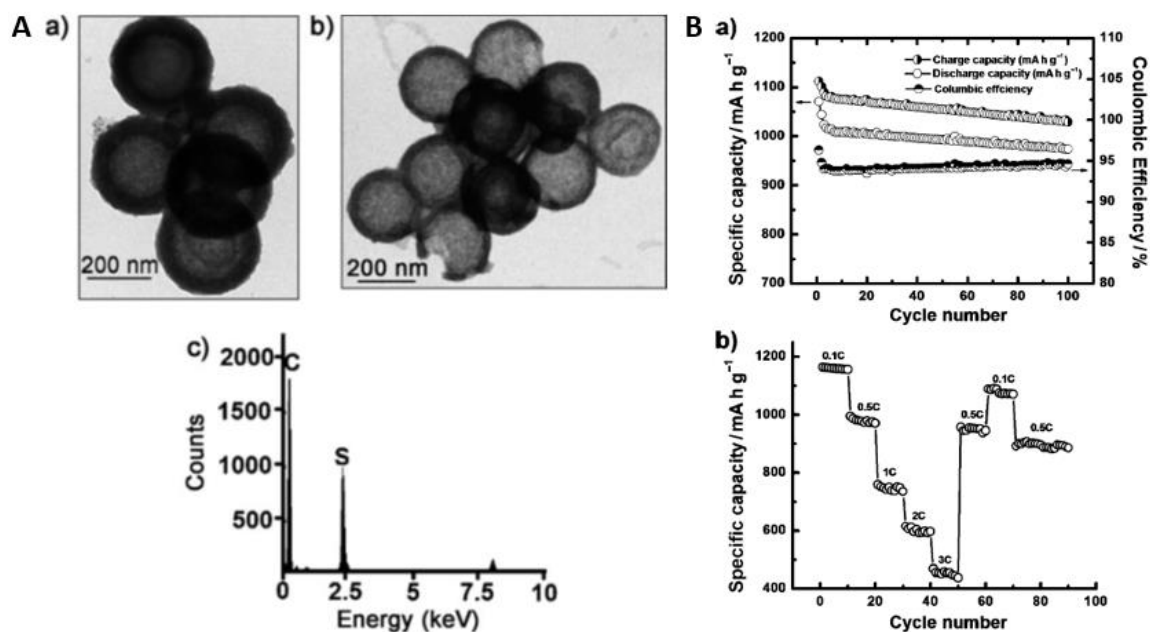
Figure 1-9. TEM images of a) mesoporous carbon hollow spheres b) C@S nanocomposite and c) EDX analysis of C@S nanocomposite showing the presence of sulfur B. a) Cycle life and b) rate

capability of C@S nanocomposite cells. Cycle life was carried out at a constant 0.5 C rate of discharge and charge.[15]

1.3.2 Fullerene-sulfur composites

A fullerene carbon molecule is entirely composed of carbon atoms, in 0D, 1D, or 2D form. In particular, due to their superb electrical conductivity and projected low cost, carbon nano-tubes (CNTs) and graphene have gained tremendous interest not only in research community but also in industry to form high-performance composites in a wide range of applications. When used to form hybrids with sulfur, CNTs or graphene is expected to greatly enhance electron conduction in the composites. Besides, surface decorations on CNTs or graphene were also explored to strengthen the interaction with polysulfides and thus improve battery performance.
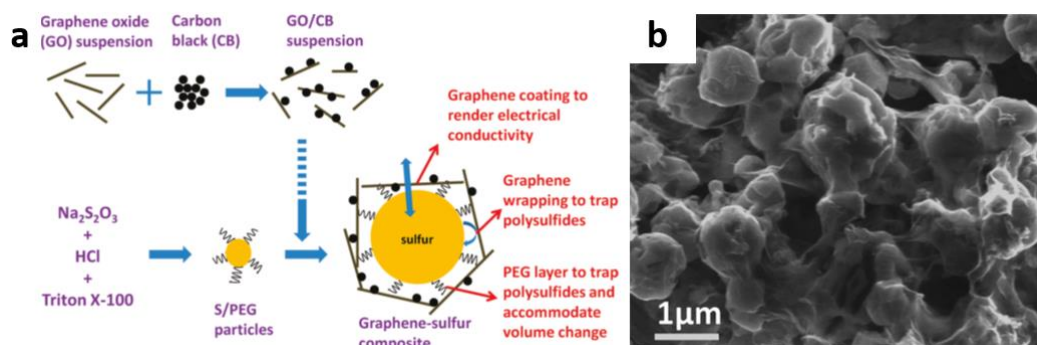
Figure 1-20. (a) Schematic of the synthesis steps for a graphene-sulfur composite, with a proposed schematic structure of the composite. (b) SEM characterization of graphene-sulfur composite.[16]

The graphene-sulfur composite material was synthesized by wrapping poly(ethylene glycol) (PEG) coated submicrometer sulfur particles with mildly oxidized graphene oxide sheets decorated by carbon black nanoparticles.[16] The PEG and graphene coating layers are important to accommodating volume expansion of the coated sulfur particles during discharge, trapping soluble polysulfide intermediates, and rendering the sulfur particles electrically conducting. The resulting graphene-sulfur composite showed high and stable specific capacities up to 600 mAh/g

over more than 100 cycles, representing a promising cathode material for rechargeable lithium batteries with high energy density.

Quasi-two dimensional graphene oxide (GO) was reported to serve as conductive substrate for sulfur deposition.[17] Chemical deposition of sulfur provides intimate contact between sulfur and carbon, which would not necessarily be the case for ball milling and thermal treatment (melt-diffusion). GO contains various kinds of functional groups on the graphene sheets, which can have strong adsorption to anchor sulfur atoms and effectively prevent the subsequently formed lithium polysulfides from dissolving into the electrolyte during cycling. X-ray absorption spectroscopy (XAS) measurement revealed that hydroxyl and epoxy groups could enhance the binding of S to the C atoms due to the induced ripples by functional groups, showing the important roles of functional groups in extending the cycle life of sulfur electrodes.
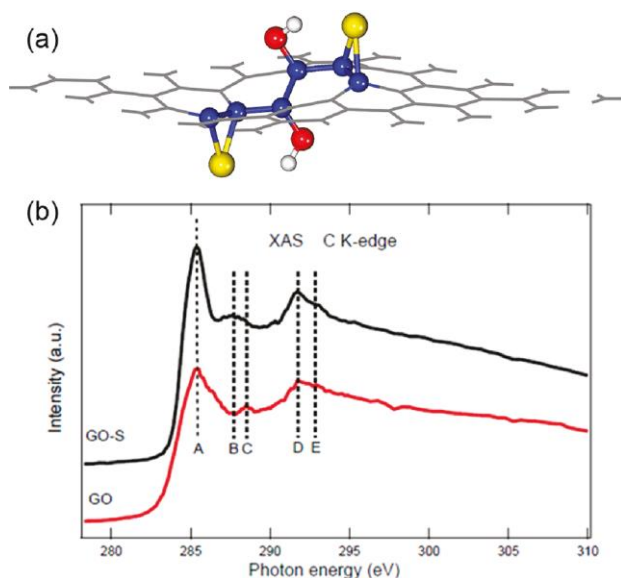
Figure 1-31. (a) Representative pattern of GO immobilizing S. The hydroxyl enhances the binding of S to the C-C bond due to the induced ripples by epoxy or hydroxyl group. Yellow, red, and white balls denote S, O, and H atoms, respectively, while the others are C atoms. Note that the C atoms bonding to S or O are highlighted as blue balls. (b) C K-edge XAS spectra of GO and GO-S nanocomposites after heat treatment in Ar at 155 C for 12 h.[17]

Secondary structures based on fullerene building blocks were proposed for their applications in Li-S batteries as well. For example, vertically aligned CNT arrays were employed as bi-functional substrates for sulfur cathode, serving as both conductive network and current collector.[18] This binder-free electrode design yielded exceptional electron conduction and excellent battery performance at high current conditions.
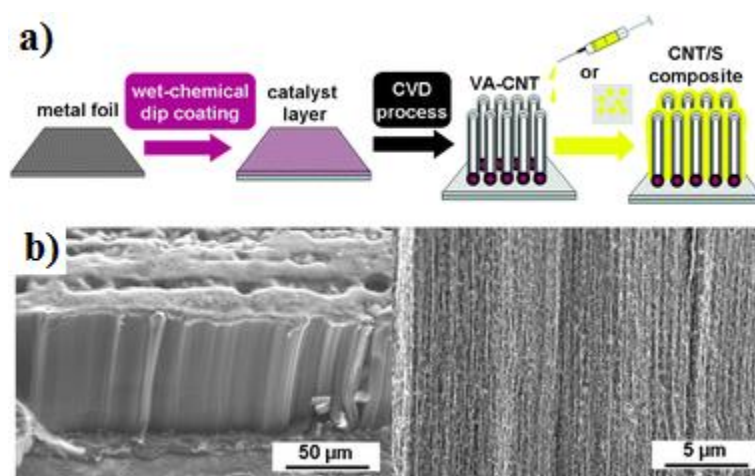
Figure 1-42. (a) Scheme of electrode preparation comprising the wet-chemical dip-coating step, the chemical vapor deposition and the sulfur infiltration by solution or melt infiltration. (b) SEM images of as-deposited carbon nanotubes.

1.3.3 Conductive polymer-sulfur composites
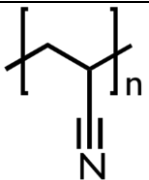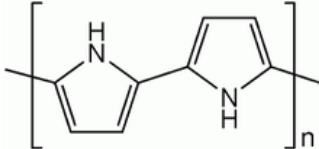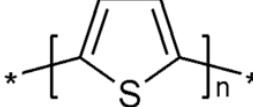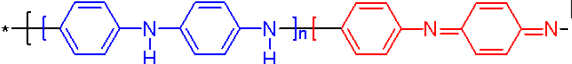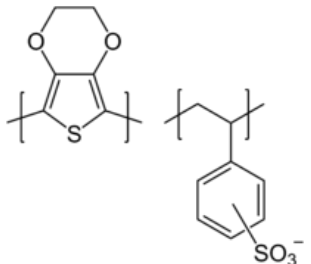
Conductive polymers are organic polymers that conduct electrons. According to the mechanism of electron conduction, conductive polymers can be divided into two groups. Redox polymers propagate electron through electron hopping between neighboring redox sites; while intrinsically conducting polymers exhibit movement of delocalized electrons through conjugated systems. They are extensively explored for the applications in Li-S batteries. Due to easy dispersion of their polymer monomers in solution and mild temperature for polymerization, synthesis of conductive polymer-sulfur composites is very versatile. Among many other designs, one interesting example is conductive polymer coating on sulfur particles. Conformal coating on sulfur with conductive materials is the most straightforward method to improve conductivity and confine sulfur species during battery cycles, but is difficult to realize using other conductive materials due to the physical and chemical volatility of sulfur.

Conductive polymer-sulfur composites can be formed by grind-mixing the two components,[30] depositing sulfur onto polymer,[20,26,29,38] or coating sulfur particles with polymers in solution phase.[25,32,36,37,39]. Furthermore, conductivity enhancers such as CNTs and graphene can be uniformly dispersed in these systems to form tri-constituent composites to enhance battery performance at high current density, thanks to the facile synthesis of conductive polymers.[21,23,27,31,35] In the case of core-shell coating designs, conductive polymer coating on sulfur particles didn't facilitate a high capacity or eliminate capacity fading. The reasons may include: 1) the coating is not conformal or complete on sulfur particles; 2) the relatively poor mechanical property of conductive polymers may not sustain the volume expansion of sulfur during battery cycling; 3) the relatively loose structure of conductive polymer may be permeable for electrolyte, as well as polymer diffusion.

Among these conductive polymers, PAN exhibits unique chemical and electrochemical properties when forming composite with sulfur. PAN itself actually is not conductive. Upon reaction with sulfur, PAN is dehydrogenated and forms conjugated structure, which makes the polymer conductive. Fanous et al. proposed that sulfur exists as side chains bonded to the backbone of the polymer in the composite, rather than in elemental state.[19] This theory may explain two unique behaviors of this composite observed in battery performance. First, when using carbonate-based electrolyte systems and elemental sulfur in the cathode, the battery would quickly fail due to reaction between the electrolyte and polysulfides. However, carbonate-based electrolyte systems are compatible with PAN-sulfur composite.[22] This indicates elemental indeed doesn't exist in the composite and polysulfides may not have formed during battery cycling. Second, when using PAN-sulfur composite as the cathode material, the charge-discharge profile is different from those when elemental sulfur is contained in the cathode. This indicates a different reaction mechanism of this composite in the battery.

Table 1-1. A summary of conductive polymers applied in Li-S batteries

Polymer Name	Chemical Structure	Reference
Polyacrylonitrile (PAN)		[19–24]
Polypyrrole		[25–35]
Polythiophene		[36,37]
Polyaniline (PANi)		[28,38,39]
PDOT:PSS		[40]

1.4 Development of electrolyte for Li-S batteries

Electrolyte is the media used to connect the cathode and anode and to transfer lithium ions in between. With lithium salts dissolved in liquid solvents, liquid electrolyte is the most technologically mature and widely adopted type of electrolyte used in various cell configurations, including cylindrical 18650 cell, pouch cells, and coin cells. Other types of electrolyte may be used occasionally for special needs. For example, solid (ceramic) electrolyte is used in thin film batteries; gel-polymer electrolyte is gaining its applications in portable devices for their high packing efficiency. Liquid electrolyte is comprised of two components: lithium salt and liquid solvent. It saturates the two electrodes and fills the space in between. The electrolyte is critical for the battery performance. The interface it forms with electrode surfaces, as well its ion transfer properties, determines not only the output energy but also battery safety. Indeed, electrolyte development was once the bottleneck technology for commercializing lithium ion batteries based on graphite anode, before settling on the current system of $LiPF_6$ dissolved in EC-containing solvents. Also, the choice of electrolyte system should depend on the choice of electrode materials and the chemistry between the electrolyte and electrode. Good electrolyte should embody the following criteria: 1) a good ionic conductor and electric insulator; 2) a wide electrochemical window that at least covers the working potentials of the two electrodes; 3) Inert to all contacting components in the battery; 4) great safety properties, such as thermal stability, low toxicity, etc.)

1.4.1 Introduction to electrolyte solvents

The options available for electrolyte solvents are actually very limited based on the strict requirements for electrolyte systems. 1) To get high ionic conductivity, the solvents need to have high dielectric constants and low viscosity. High dielectric constants indicate more polarity for the solvent molecule and stronger capacity to dissolve lithium salts. On the other hand, solvents with lower viscosity have better mass transfer property to facilitate ion conduction. However, these two parameters are often inversely related, as more polar molecules result in solvents with higher viscosity. As a result, successful electrolyte systems adopt two or more solvent components. One can well dissolve salts and the other lowers the viscosity. Combined, they provide good overall battery performance. 2) Solvents should have a wide electrochemical window to prevent side reaction during at the working potentials of batteries. This requirement rules out any solvents that give out protons. Despite of their polar structure and the ability to dissolve a variety of salts, they are only stable in an electrochemical window <2V because of the released protons and the corresponding anions. Such narrow electrochemical windows are not useful for battery applications. In other words, all electrolyte solvents are aprotic, meaning they can't generate protons in the solution. 3) Suitable solvents should also have a wide liquid range. The electrolyte should stay in liquid in working conditions. Solidified electrolyte would simply block ion transfer and fail the batteries. Commonly used electrolyte solvents fall into three categories: carbonates, ethers, and esters.

Table 1-2. Organic carbonates and esters as electrolyte solvents

Solvent	Structure	M. Wt	$T_m/\,^{\circ}C$	$T_b/\,^{\circ}C$	η/cP 25 $^{\circ}C$	ε 25 $^{\circ}C$	Dipole Moment/debye	$T_f/\,^{\circ}C$	d/gcm^{-3}, 25 $^{\circ}C$
EC		88	36.4	248	1.90, (40 $^{\circ}C$)	89.78	4.61	160	1.321
PC		102	-48.8	242	2.53	64.92	4.81	132	1.200
BC		116	-53	240	3.2	53			
γBL		86	-43.5	204	1.73	39	4.23	97	1.199
γVL		100	-31	208	2.0	34	4.29	81	1.057
NMO		101	15	270	2.5	78	4.52	110	1.17
DMC		90	4.6	91	0.59 (20 $^{\circ}C$)	3.107	0.76	18	1.063
DEC		118	-74.3 [a]	126	0.75	2.805	0.96	31	0.969
EMC		104	-53	110	0.65	2.958	0.89		1.006
EA		88	-84	77	0.45	6.02		-3	0.902
MB		102	-84	102	0.6			11	0.898
EB		116	-93	120	0.71			19	0.878

Table 1-3. Organic ethers as electrolyte solvents

Solvent	Structure	M. Wt	$T_m/\,^{\circ}C$	$T_b/\,^{\circ}C$	η/cP 25 $^{\circ}C$	ε 25 $^{\circ}C$	Dipole Moment/debye	$T_f/\,^{\circ}C$	d/gcm^{-3}, 25 $^{\circ}C$
DMM		76	-105	41	0.33	2.7	2.41	−17	0.86
DME		90	-58	84	0.46	7.2	1.15	0	0.86
DEE		118	-74	121				20	0.84
THF		72	-109	66	0.46	7.4	1.7	-17	0.88
2-Me-THF		86	-137	80	0.47	6.2	1.6	-11	0.85
DOL		74	-95	78	0.59	7.1	1.25	1	1.06
4-Me-1,3-DL		88	-125	85	0.60	6.8	1.43	-2	0.983
2-Me-1,3-DL		88			0.54	4.39			

Carbonate solvents have always be the focus electrolyte development. Most notably, these solvents possess high dielectric constant that enables them to dissolve a wide range of lithium salts. Propylene carbonate (PC) first attracted attention as early as 1958 when lithium was demonstrated to electrodeposit from a solution of LiClO$_4$ in PC. Besides the high dielectric constant that carbonates commonly have, PS has a wide liquid range between -48.8°C and 242°C, making it extremely suitable for battery applications in normal conditions. A major drawback of using PC as solvents came to the realization that PC continually react with lithium metal (the anode material of choice at the time) and results in poor cycling performance. The coulombic efficiency is lower than 85% because of this side reaction.

Ether-type solvents then gained popularity afterward, up to early 90's, because they show much better stability with lithium metal anode. During this time, lithium metal still was considered the best candidate as anode material. Compared with PC, ethers can form much better SEI layers on the lithium metal and significantly increases coulombic efficiency.

Carbonates again became the focus of research in early 90's as lithium ion batteries were commercialized. In these batteries, lithium metal was replaced by graphite on the anode, which is intrinsically a safer design due to lower reactivity of graphite and lithiated graphite than lithium metal. Similar to the intercalation chemistry on the cathodes, lithium would intercalate into and de-intercalate out of the graphite host during battery cycling. The operating potential of the graphite anode is 0-0.2V higher than the lithium metal anode. This mechanism of lithium shuttling between the cathode and anode host was termed "rocking chair technology". The enabler of this technology is the use of ethylene carbonate (EC) as one the solvents components. Previously, no alternatives could be found to the troublesome lithium metal anode. For graphite, solvents would intercalate into and decompose the graphite structure. It came as a surprise to use

EC as a solvent component as EC is in solid at ambient temperature. Its melting temperature is 36.4°C. As a result, EC can only be used as a co-solvent while other solvent(s) are used to dissolve both EC and lithium salt. An EC/PC mixture was used as electrolyte solvents in the lithium ion batteries in those years. Although their molecule structures are only slightly different, EC was demonstrated to form very stable SEI layer on graphite anode than PC by Dahn. The underneath mechanism is still under debate.
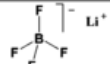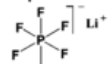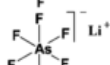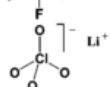
The state-of-the-art electrolyte system in today's lithium ion batteries may be a complex system containing over 5 components. A notable improvement from the EC/PC system is the introduction of esters as co-solvents to replace PC. Esters, such DMC, DEC, and DME, were found to effectively suppress the melting point of EC and result in a wider liquid range for the electrolyte, more suitable for battery applications. With a low viscosity, the resulting electrolyte is more ionically conductive. What's more, the addition of these esters was found to widen the electrochemical window of the electrolyte, making it more versatile for various electrode materials and a safer choice. Other new electrolyte components are mostly for safety concerns, including the use of flame-retardants.

1.4.2 Introduction to electrolyte salts

Requirements for ideal electrolyte salts include: 1) The salts should have a reasonable solubility in the limited options of electrolyte solvents, in order to get a high ion conductivity. 2) The cations and anions of the salts should remain stable in the potential range of battery operation. 3) The salts should be non-toxic. Since the choice of salts is based on the solvents, the number of suitbale electrolyte salts available is even scarcer than that for the solvents. Common salts are listed in the table 1-4. These choices of salts can be divided into two categories. The first group (including $LiPF_6$, $LiClO_4$, $LiBF_4$, and $LiAsF_6$) are based on Lewis acid; and the second group (including Li Triflate, LiTFSI, and Li Beti) are based on the conjugate bases of organic super acids. For example, $LiPF_6$ can be viewed as F- complexed by the Lewis acid PF_5, which well distributes the negative charge on the whole anion and results in better solubility in non-polar solvents; while the anion of Li Triflate also evenly distributes the negative charge due to the strongly electron-withdrawing conjugate bases.

$LiPF_6$ is the electrolyte salt of choice in state-of-the-art lithium ion batteries, not as a perfect choice but as the most balanced one. Its ion conductivity is lower than that of $LiAsF_6$ in PC solution. Its reaction with even trace amount of moisture in the electrolyte can generate serious corrosion of battery components and gaseous products to plague battery performance. This sensibility to moisture requires extra care during product purification and battery fabrication. However, it still excels in most of the categories as an electrolyte salt, including conductivity, electrochemical stability, among others.

Table 1-4. Lithium salts as electrolyte solute

Salt	Structure	M. Wt	T_m/°C	$T_{decomp.}$ /°C in solution	Al-corrosion	σ /mScm⁻¹ (1.0 M, 25 °C)	
						in PC	in EC/DMC
LiBF₄		93.9	293 (d)	> 100	N	3.4 [a]	4.9 [c]
LiPF₆		151.9	200 (d)	~ 80 (EC/DMC)	N	5.8 [a]	10.7 [d]
LiAsF₆		195.9	340	> 100	N	5.7 [a]	11.1 [e]
LiClO₄		106.4	236	>100	N	5.6 [a]	8.4 [d]
Li Triflate	$Li^+ CF_3SO_3^-$	155.9	>300	>100	Y	1.7 [a]	
Li Imide	$Li^+ [N(SO_2CF_3)_2]^-$	286.9	234 [b]	>100	Y	5.1 [a]	9.0 [e]
Li Beti	$Li^+ [N(SO_2CF_2CF_3)_2]^-$				N		

1.4.3 Electrolyte development for Li-S batteries

As designs of Li-S batteries are still based on lithium metal anode in the foreseeable future, ether-type solvents are the best choice for electrolyte due to their stability with lithium metal and the suppression of dendrite growth on lithium metal.[41] Also, carbonate solvents are found to react with polysulfide and fail the battery in the first few cycles.[7]

Early explores of Li-S batteries are mostly based on THF as an electrolyte solvent.[42,43] Notably, when using $LiClO_4$ salt dissolved in a mixture of THF and toluene, a Li-S battery showed 95% utilization rate for the first discharge.[43] Recent research advances in this system couldn't even approach this value. However, likely due to a poor cycling performance, results for following cycles were not shown in these reports.

DOL was shown to form an excellent SEI layer on lithium metal anode and demonstrated near 100% charge/discharge efficiency for lithium metal anode.[44] DOL was then introduced as an electrolyte solvent for Li-S batteries in 1989 by Peled and showed much improved cycling performance.[43] In recent researches on Li-S batteries, DOL paired with DME co-solvent and LiTFSI salt is practically the standard for electrolyte. Co-solvents with higher dielectric constants, such as DME, have a higher solubility for lithium salt and can effectively increase the ion conductivity of the electrolyte. The ratio between the two solvent components may also affect battery performance.[45] Long-chained ethers were explored as a co-solvent or the sole solvent for Li-S batteries as well, such as TEGDME (tetraethylene glycol dimethyl ether) and PEGDME (polyethylene glycol dimethyl ether).[15,17,46] These ethers proved to be stable with stable with lithium metal anode. More importantly, cycling performance appeared extremely well with high capacity retention over long cycles, likely due to the low diffusion of polysulfides in these highly

viscous solvents. However, the high viscosity also severely limits the battery performance at high current density.

As for the electrolyte salts in Li-S batteries, LiTFSI is used in most of the recently publications due to its high conductivity, stability, and low toxicity. Li triflate is used by certain groups as well. In comparison, LiTFSI has much higher ion conductivity. $LiClO_4$ is occasionally used but its high reactivity causes safety concerns. $LIPF_6$ has limited solubility in ether-type solvents and is not used. Reference showed that different salts don't affect battery performance much.[7]

1.4.4 LiNO3 as electrolyte additive for Li-S batteries

One of the most important discoveries for the recent development of Li-S batteries is the benefit of using $LiNO_3$ as electrolyte additive. Polysulfides are inevitably generated in Li-S batteries as reaction intermediates and can readily dissolve into the electrolyte. These dissolved polysulfides diffuse and lose electrons to the lithium anode and retrieve electrons when diffused back to the cathode, causing an internal short-circuit and suppressing charge efficiency at a low level. Such phenomenon is termed the polysulfide shuttle effect.[47] The resultant low charge efficiency and safety concerns seriously prevent Li-S batteries from practical applications, along with other problems. Pioneering works tried delicate coating containing N element on lithium metal anode and showed favorable effect. Sion Power Inc. then first introduced $LiNO_3$ as an electrolyte additive for Li-S batteries in their 2008 patent and demonstrated completely dampened polysulfide shuttle effect with 100% charge efficiency during cycling. This effect has been repeated in many publications. The use of $LiNO_3$ as electrolyte additive almost became a standard in recent development of Li-S batteries.

The mechanism of this effect is still under debate. Zhang found that, when the lithium metal immersed in the electrolyte containing $LiTFSI/LiNO_3/DOL/DME$, a flat and homogeneous surface film (SEI) was obtained.[48] The top layer formed with $LiNO_3$ consists of both inorganic species such as LiN_xO_y and organic species such as ROLi and $ROCO_2Li$. With the increasing depth, the order of nitrogen in reduction products becomes lower, from $Li_2N_2O_2$ to Li_3N. Under the top layer, the film manly consists of $ROCO_2Li$, Li_2O, LiN_xO_y and Li_3N. These species prevent the continuous electron transfer from lithium metal to polysulfides and electrolyte solutions. However, due to the unstable SEI on the lithium metal anode, $LiNO_3$ is continually consumed as fresh surface of lithium metal exposes during deposition (charge process). After certain number

of battery cycles, LiNO$_3$ would be used up in the battery and the coulombic efficiency would

plunge as when LiNO$_3$ is not used.

Reference (Chapter 1)

[1]   Y. V. Mikhaylik, J. R. Akridge, *J. Electrochem. Soc.* **2003**, *150*, A306.

[2]   J. R. Akridge, Y. V Mikhaylik, N. White, *Solid State Ionics* **2004**, *175*, 243–245.

[3]   X. Ji, K. T. Lee, L. F. Nazar, *Nat. Mater.* **2009**, *8*, 500–506.

[4]   N. a. Cañas, S. Wolf, N. Wagner, K. A. Friedrich, *J. Power Sources* **2013**, *226*, 313–319.

[5]   M. U. M. Patel, R. Demir-Cakan, M. Morcrette, J.-M. Tarascon, M. Gaberscek, R. Dominko, *ChemSusChem* **2013**, *6*, 1177–81.

[6]   C. Barchasz, F. Molton, C. Duboc, J.-C. Leprêtre, S. Patoux, F. Alloin, *Anal. Chem.* **2012**, *84*, 3973–3980.

[7]   J. Gao, M. A. Lowe, Y. Kiya, H. D. Abruña, *J. Phys. Chem. C* **2011**, *115*, 25132–25137.

[8]   M. S. Whittingham, *Chem. Rev.* **2004**, *104*, 4271–301.

[9]   S.-E. Cheon, K.-S. Ko, J.-H. Cho, S.-W. Kim, E.-Y. Chin, H.-T. Kim, *J. Electrochem. Soc.* **2003**, *150*, A796–A799.

[10]   S.-E. Cheon, K.-S. Ko, J.-H. Cho, S.-W. Kim, E.-Y. Chin, H.-T. Kim, *J. Electrochem. Soc.* **2003**, *150*, A800–A805.

[11]   Y. J. Choi, B. S. Jung, D. J. Lee, J. H. Jeong, K. W. Kim, H. J. Ahn, K. K. Cho, H. B. Gu, *Phys. Scr.* **2007**, *T129*, 62–65.

[12]   Y. Diao, K. Xie, S. Xiong, X. Hong, *J. Electrochem. Soc.* **2012**, *159*, A421–A425.

[13]   C. Liang, N. J. Dudney, J. Y. Howe, *Chem. Mater.* **2009**, *21*, 4724–4730.

[14]   S. Xin, L. Gu, N.-H. Zhao, Y.-X. Yin, L.-J. Zhou, Y.-G. Guo, L.-J. Wan, *J. Am. Chem. Soc.* **2012**, *134*, 18510–18513.

[15]   N. Jayaprakash, J. Shen, S. S. Moganty, A. Corona, L. a. Archer, *Angew. Chemie* **2011**, *123*, 6026–6030.

[16]   H. Wang, Y. Yang, Y. Liang, J. T. Robinson, Y. Li, A. Jackson, Y. Cui, H. Dai, *Nano Lett.* **2011**, *11*, 2644–2647.

[17]   L. Ji, M. Rao, H. Zheng, L. Zhang, *J. Am. Chem. Soc.* **2011**, *133*, 18522–18525.

[18]   S. Dorfler, M. Hagen, H. Althues, J. Tubke, S. Kaskel, M. J. Hoffmann, *Chem. Commun.* **2012**, *48*, 4097–4099.

[19]   J. Fanous, M. Wegner, J. Grimminger, Ä. Andresen, M. R. Buchmeiser, *Chem. Mater.* **2011**, *23*, 5024–5028.

[20]   J. Wang, J. Yang, J. Xie, N. Xu, *Adv. Mater.* **2002**, *050*, 963–965.

[21]   L. Yin, J. Wang, J. Yang, Y. Nuli, *J. Mater. Chem.* **2011**, *21*, 6807.

[22]   L. Wang, X. He, J. Li, M. Chen, J. Gao, C. Jiang, *Electrochim. Acta* **2012**, *72*, 114–119.

[23]   L. Yin, J. Wang, F. Lin, J. Yang, Y. Nuli, *Energy Environ. Sci.* **2012**, *5*, 6966.

[24]   L. Wang, X. He, J. Li, J. Gao, J. Guo, C. Jiang, C. Wan, *J. Mater. Chem.* **2012**, *22*, 22077.

[25]   J. Wang, J. Chen, K. Konstantinov, L. Zhao, S. Ng, G. Wang, Z. Guo, H. Liu, *Electrochim. Acta* **2006**, *51*, 4634–4638.

[26]   M. Sun, S. Zhang, T. Jiang, L. Zhang, J. Yu, *Electrochem. commun.* **2008**, *10*, 1819–1822.

[27]   S. Bose, T. Kuila, M. E. Uddin, N. H. Kim, A. K. T. Lau, J. H. Lee, *Polymer (Guildf).* **2010**, *51*, 5921–5928.

[28]   L. Qiu, S. Zhang, L. Zhang, M. Sun, W. Wang, *Electrochim. Acta* **2010**, *55*, 4632–4636.

[29]   X. Liang, Y. Liu, Z. Wen, L. Huang, X. Wang, H. Zhang, *J. Power Sources* **2011**, *196*, 6951–6955.

[30]   Y. Zhang, Z. Bakenov, Y. Zhao, A. Konarov, T. N. L. Doan, M. Malik, T. Paron, P. Chen, *J. Power Sources* **2012**, *208*, 1–8.

[31]   X. Liang, Z. Wen, Y. Liu, H. Zhang, J. Jin, M. Wu, X. Wu, *J. Power Sources* **2012**, *206*, 409–413.

[32]   Y. Fu, A. Manthiram, *J. Phys. Chem. C* **2012**, *116*, 8910–8915.

[33]   Y. Fu, Y.-S. Su, a. Manthiram, *J. Electrochem. Soc.* **2012**, *159*, A1420–A1424.

[34]   Y. Fu, A. Manthiram, *Chem. Mater.* **2012**, *24*, 3081–3087.

[35]   J. Wang, L. Lu, D. Shi, R. Tandiono, Z. Wang, K. Konstantinov, H. Liu, *Chempluschem* **2013**, *78*, 318–324.

[36]   F. Wu, S. Wu, R. Chen, J. Chen, S. Chen, *Electrochem. Solid-State Lett.* **2010**, *13*, A29–A31.

[37]   F. Wu, J. Chen, R. Chen, S. Wu, L. Li, S. Chen, T. Zhao, *J. Phys. Chem. C* **2011**, *115*, 6057–6063.

[38]   L. Xiao, Y. Cao, J. Xiao, B. Schwenzer, M. H. Engelhard, L. V Saraf, Z. Nie, G. J. Exarhos, J. Liu, *Adv. Mater.* **2012**, *24*, 1176–1181.

[39]   G.-C. Li, G.-R. Li, S.-H. Ye, X.-P. Gao, *Adv. Energy Mater.* **2012**, *2*, 1238–1245.

[40]   Y. Yang, G. Yu, J. Cha, H. Wu, *ACS Nano* **2011**, *5*, 9187–9193.

[41]   K. Xu, *Chem. Rev.* **2004**, *104*, 4303–417.

[42]   R. D. Rauh, K. M. Abraham, G. F. Pearson, J. K. Surprenant, S. B. Brummer, *J. Electrochem. Soc.* **1979**, *126*, 523–527.

[43]   E. Peled, Y. Sternberg, *J. Electrochem. Soc.* **1989**, *136*, 1621–1625.

[44]   D. Aurbach, E. Zinigrad, Y. Cohen, H. Teller, *Solid State Ionics* **2002**, *148*, 405–416.

[45]   W. Wang, Y. Wang, Y. Huang, C. Huang, Z. Yu, H. Zhang, A. Wang, K. Yuan, *J. Appl. Electrochem.* **2009**, *40*, 321–325.

[46]   D.-R. Chang, S.-H. Lee, S.-W. Kim, H.-T. Kim, *J. Power Sources* **2002**, *112*, 452–460.

[47]   Y. V Mikhaylik, J. R. Akridge, *J. Electrochem. Soc.* **2004**, *151*, A1969–A1976.

[48]   S. S. Zhang, *Electrochim. Acta* **2012**, *70*, 344–348.

Chapter 2

Optimizing pore structure of porous carbon to enhance battery performance of carbon-sulfur composites

2.1 Introduction

Development of porous carbon-sulfur (C-S) composites is one of the main focuses researches on lithium-sulfur (Li-S) batteries. Well-designed porous carbon can effectively enhance utilization rate of sulfur (i.e. the active battery material) and stabilize capacity of this highly expected battery system. Due to the physical and chemical volatility of sulfur, synthesis of sulfur-composites is limited by various factors. Nazar's group pioneered designing C-S composites by using mesoporous carbon, CMK-3, as a conductive scaffold to contain sulfur, taking advantage of sulfur's volatility.[1] At a mildly elevated temperature (~155°C when its viscosity at the lowest), sulfur would liquefy and diffuse into the cylindrical mesopores of CMK-3 (3-4 nm in diameter) and form a uniform composite. The suppression of sulfur particle size and the intimate contact between carbon and sulfur result in a high utilization rate (i.e. a high specific capacity of sulfur). Meanwhile, a high surface area generally accompanies the high porosity of such carbon, which promotes polysulfides adsorption and improves cycle stability. It was later found that tuning the nano-structures of carbon-sulfur composites could effectively affect the performance and even alter the chemistry of the batteries. Liang introduced hierarchically porous carbon as the conductive scaffold for sulfur.[2] The synergy of micropores (<2 nm) and mesopores (7.3 nm) improved battery performance as the nanostructure was optimized to allow stronger adsorption in micropores and easier mass transport in mesopores. Microporous carbon was recently demonstrated to completely inhibit the diffusion of polysulfides by confining sulfur with shorter chains (S_2 and S_4, rather than S_8) in the designed micropores (pore size < 0.5 nm).[3] However, this design comes with fatal shortcomings as the output voltage is severely lowered and

sulfur content in the composite can hardly exceed 50%. Indeed, due to the high potentials of Li-S batteries and the versatility of synthesizing porous carbon, recently year saw an outbreak of applying C-S composites to Li-S batteries in research literature.[4–9]

For C-S composites in Li-S battery applications, the pore volume and surface area of the carbon scaffolds are two critical parameters. A higher pore volume allows relatively more sulfur in the composite, which is desired for a higher capacity in theory and a lower cost of battery material. On the other hand, a higher surface area favors capacity retention due to a stronger interaction of polysulfides on the carbon surface. Unfortunately, the pore volume and surface area are two competing values, which are largely determined by the pore structure (or its size distribution) of the material. Larger pores generally yield high pore volumes and low surface areas, while smaller pores lead to the opposite trend. The pore structure of carbon scaffolds should be optimized to improve the performance of Li-S batteries and it remains a challenge to achieve satisfactory battery performance with high sulfur content in the cathode material. In spite of demonstrated progresses in battery performance and design novelties, many previous reports comprised on sulfur content in the designed composites due limited pore volumes of porous carbon. It's rare to see sulfur content above 70%.

Herein, a highly porous carbon (HPC) design is explored as the carbon scaffold for sulfur and applied in Li-S batteries. While an ultra-high pore volume of 3.2 cm^3/g was obtained, the pore size was largely controlled below 20nm, which contributed to a high surface area and suppressed the particle size of sulfur. As a result, the HPC-sulfur composite exhibited excellent battery performance even at notably high sulfur content of 80wt.%.

2.2 Experimental section

Synthesis of resol polymer precursor: The resin precursor (Mw <500) was prepared according to reported method in the literature.[10] In a typical procedure, 12.2 g of phenol was melted at 40-42 °C in a flask and mixed with 2.6 g of 20 wt% NaOH aqueous solution under stirring for10 min. Then, 20.1 g of formalin (37 wt% formaldehyde) was added dropwise at 45 °C. Upon further stirring for 1h at 72 °C, the mixture was cooled to room temperature and the pH value was adjusted to about 7.0 by addition of HCl solution. After water was removed in a rotary evaporator at 50 °C, the final product was dissolved in ethanol to form a 20 wt% ethanolic solution.

Synthesis of HPC: In a typical preparation of HPC, 1.65g block copolymer F127 (Mw=12600, $PEO_{106}PPO_{70}PEO_{106}$, Sigma-Aldrich) was first dissolved in 8g ethanol with 1.0g HCl (0.2 M), then 5ml of colloidal silica ST-0 (Nissan Chemical) was added, and stirred for 1h at 40°C to afford a clear solution. Next, 2.08g TEOS and 5.5g resin solution (20 wt%) were added in sequence, stirring for 30 minutes in between. After being stirred for 2 h, the mixture was transferred into large petri dishes. The mixture was left overnight to evaporate ethanol and then heated for 24 h at 100 °C in an oven to thermopolymerize. The as-made products (films or membranes) were scraped from the dishes. Calcination was carried out sequentially in a tubular furnace, first at 350 °C for 3 h and next at 900 °C for 2 h under Ar flow to get HPC-SiO_2 nanocomposites. The heating rate was 1 °C/min below 600 °C and 5 °C/min above 600 °C. The HPC nanocomposites were immersed in 2 wt% HF solutions to remove silica, leaving HPC carbon material. The as-made product was washed by distilled water several times and dried at 80 °C in an oven.

Synthesis of HPC-sulfur composites: HPC-sulfur composites with various sulfur contents can be obtained with a melt-diffusion method. Firstly, mix HPC with sulfur according to the desired sulfur content by ball-milling (300rpm for 30min). The mixture was then heated at 155°C for 8 hours in a closed container.

Characterization: The crystalline structures of the as-prepared composites were characterized by X-ray diffraction (XRD) on a Rigaku Miniflex II spectrometer. The microstructure of the composite particles was investigated with a JEOL 1200 transmission electron microscope (TEM). The surface area and pore structure were characterized by nitrogen sorption using a Micrometrics ASAP 2020 physisorption analyzer. The surface area was calculated by the Brunauer–Emmett–Teller (BET) model. The pore size distributions were derived from the adsorption branches of isotherms using the Barrett–Joyner–Halenda (BJH) model.

2.3 Results and discussion

2.3.1 Synthesis and characterization

The highly porous carbon (HPC) was synthesized by carefully choosing a tri-constituent system of pore templates, based on the synthesis of FDU15 carbon by Zhao's group.[10] **Figure 2-1** illustrates the synthesis approach for HPC. (See experimental section for details.) Briefly, HPC was synthesized through an "evaporation-induced self-assembly" process (EISA).[11] Block copolymer F127, resol precursor, TEOS (tetraethyl orthosilicate), and colloidal silica spheres were homogeneously mixed in an ethanol solution. As the solvents (ethanol and water) evaporate, the F127 molecules would self-assemble into cylindrical structures, shaping its negative phase with the remaining precursors, including the resol, TEOS, and colloidal silica. The carbon source, resin precursor, formed an open-channel structure, which would later form an open-channel structure in carbon after carbonization at 900 °C. TEOS (hydrolyzed and condensed to SiO_2 in solution), F127, and colloidal silica would be removed as templates, which created pores with sizes of <5nm, 5-10nm, 10-20nm, respectively. Although the hard-templated pores by colloidal silica should retain their sizes, the pores template by TEOS and F127 may have their sizes influenced by synthesis condition. These pores were homogeneously distributed in the open-channel structure. Finally, sulfur can be embedded into HPC by a melt-diffusion method. These composites were denoted as HPC-SX, where X is the sulfur content in a composite.
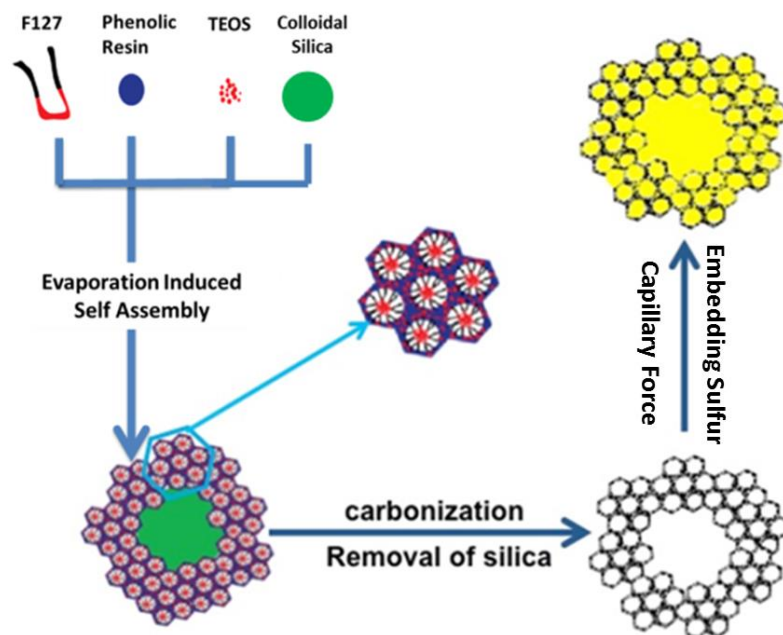
Figure 2-1. Synthesis scheme for highly porous carbon (HPC) and its sulfur composites.

The morphology and porosity of HPC were studied by transmission electron microscopy (TEM) and N_2 sorption measurement. The TEM image reveals the porous structure of HPC, which is consistent with the initial design (**Figure 2-2**). The open channels orderly distributed in the structure. The diameter of the cylindrical channels is ~7nm, created by F127, while the distance between each repeating unit of cylinder is ~10nm (cylindrical diameter plus wall thickness). This ordered structure was disrupted by voids created by colloidal silica, whose diameters are in a wide range. The pores created by hydralyzed TEOS is not visible under this magnification. More details on the porosity of the HPC material was unveiled by N_2 sorption measurement (**Figure 2-3**). This material has a high surface area of 1629 m^2/g. More importantly, the pore volume is 3.2 cm^3/g, considerably higher than most of the previous reports on porous carbon. As a comparison, the porosity parameters for CMK-3 that was used in Nazar's report are:

1976 m^2/g for surface area and 2.1 cm^3/g for pore volume. The 50% increase in pore volume helped to push up the sulfur content in C/S composite from 70w% to 80w%. The pore size distribution of the HPC material was also calculated using the BJH (*Barret-Joyner-Halenda*) model. Only a peak for pore size around 7nm was recorded. The pores in this size should have been generated by the soft template of cylindrical F127 micelles, which is consistent with TEM observation. A small hump at ~2nm on the size distribution plot should correspond to the pores template by TEOS. It should be noted that 2nm is at the lower end of the BJH model and the peak strength at this position may not represent an accurate pore population. On the other hand, the pores generated by colloidal silica are hardly discerned, possibly due to its wide range of size distribution.
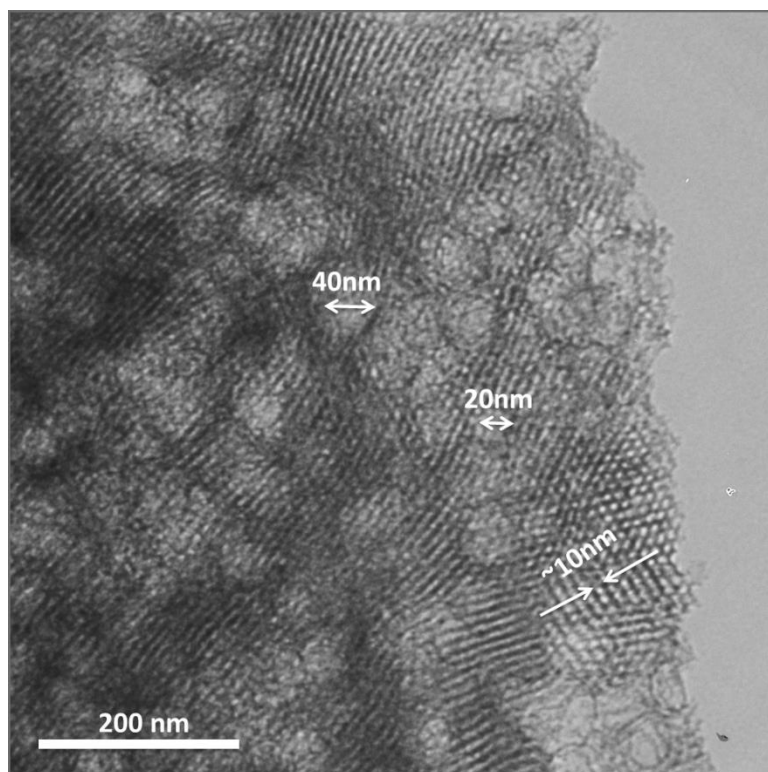
Figure 2-2. TEM image of HPC showing its pore structure.
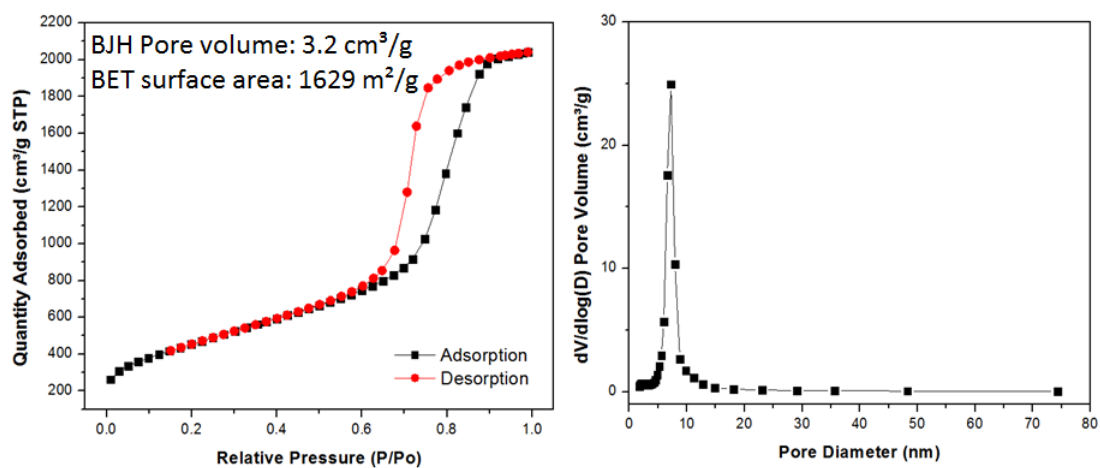
Figure 2-3. N_2 sorption isotherm (left) and calculated pore size distribution (right) for HPC.
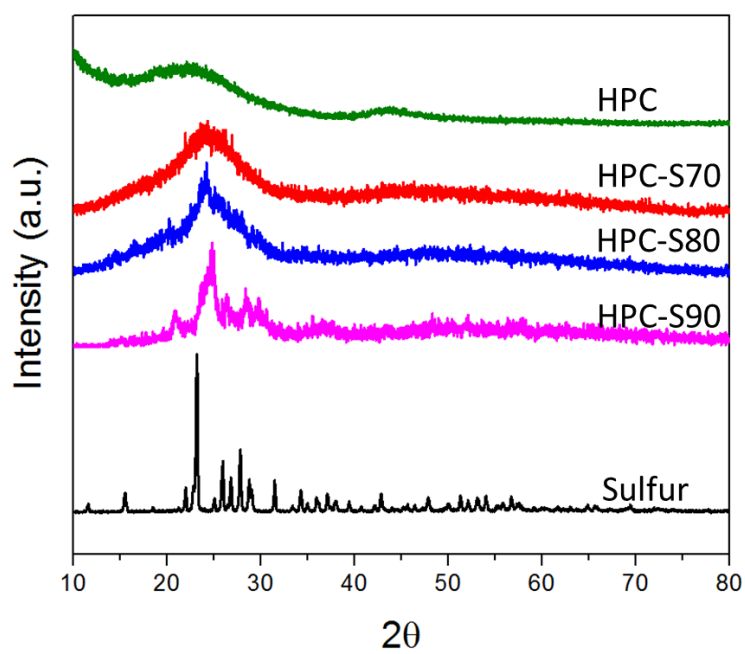
Figure 2-4. XRD patterns of HPC-sulfur composites with different sulfur contents.

To verify the good confinement of size of sulfur particles, XRD (X-ray diffraction) technique was adopted. Materials with large crystal sizes, like pure sulfur, exhibit strong diffraction patterns of X-ray due to their ordered structures. **Figure 2-4** shows the XRD patterns of HPC-sulfur composites with various sulfur contents. Composites with lower sulfur contents (HPC-S70 and HPC-S80) showed in their patterns only a broad peak at around 25°, which corresponds to amorphous carbon, while showing no peaks corresponding to elemental sulfur. In contrast, with further increased sulfur content, HPC-S90 showed several peaks that should correspond to sulfur crystals. These measurements clearly demonstrated that good confinement of sulfur in the nano-scaled pores of HPC could be achieved with up to 80% sulfur content in the composite. This is consistent with BET results on specific pore volumes of HPC. It's worth noting that sulfur peaks in the pattern of HPC-S90 don't fully match that of elemental sulfur. While elemental sulfur generally exists in its α-polymorph, it may have turned to a different polymorph during the solidification process in the HPC structure.

2.3.2 Battery testing

Half-cells battery testing was performed to evaluate these HPC-sulfur composites as cathode materials for Li-S battery applications. First of all, the battery cycling performance didn't show a monotonous trend with the sulfur content in the composites (**Figure 2-5**). The initial capacity (specific to the mass of sulfur) monotonously increased with lower sulfur content in the composites. For example, at a high current rate of C/2, HPC-S60 showed a high initial capacity close to 1200 mAh/g, indicating a high utilization rate of sulfur and a fairly complete conversion to Li_2S. This good performance can be attributed to the uniform distribution of sulfur in the porous carbon structure. As the sulfur content increases, sulfur particles may aggregate more severely, which leads to lower initial capacity. The initial capacity of HPC-S90 was less than 800 mAh/g, almost just 2/3 that of HPC-S60. However, composites with lower sulfur content may not retain capacity well. For instance, HPC-S70 showed much better capacity retention than HPC-S60, with the capacity of the former surpassing that of the latter on just the second cycle and gradually improved the lead. One explanation is that, when the sulfur content is low, more unoccupied pore space is left for the electrolyte. Consequently, relatively more polysulfides are dissolved in the electrolyte that causes a more severe loss of active material.

Meanwhile, a high pore volume is unarguably crucial. The above analysis suggests that there may be a critical value of sulfur content relative to the pore volume of a carbon scaffold when the resultant battery performance is optimum. Hence, if the pore volume is limited, reasonable performance can only be obtained with low sulfur contents.
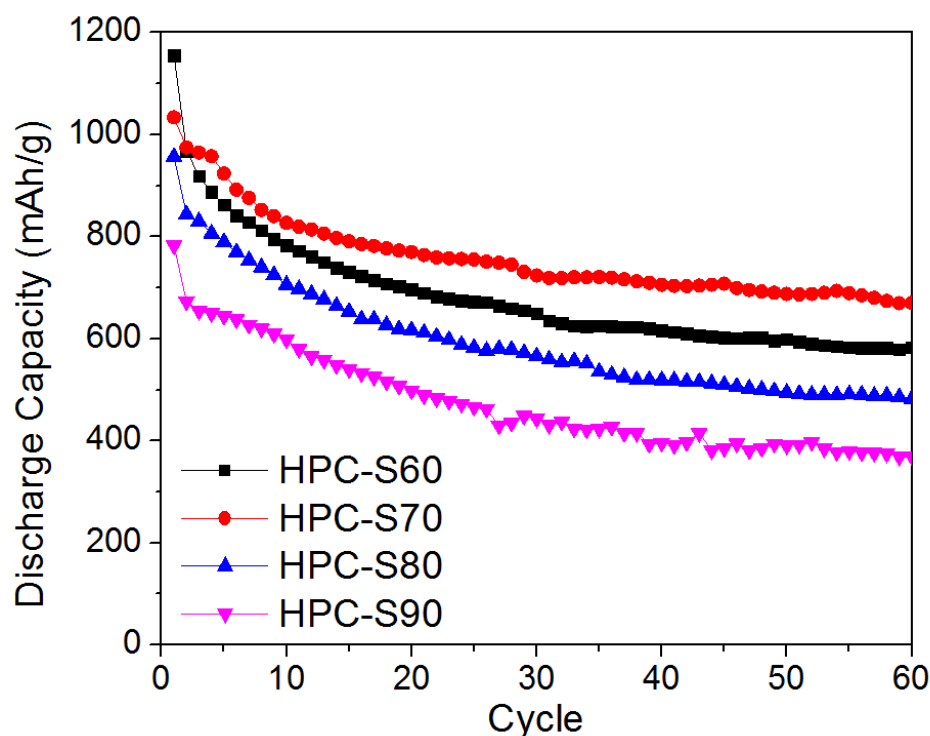
Figure 2-5. Battery cycling performance of HPC-sulfur composites with various sulfur contents. The current rate was C/2 (836 mA/g-S).

Even at a high sulfur content of 80%, HPC-S80 still exhibit excellent performance as a cathode material for Li-S battery applications. **Figure 2-6** shows the charge/discharge profiles of HPC-S80 material from half-cell battery testing at different current rates. Here, current rates are expressed in C values. 1C = 1680 mA/g, that is to charge or discharge the theoretical capacity in one hour. At a slower rate of C/10, a high discharge capacity of ~1200 mAh/g (based on sulfur) was realized, representing sulfur utilization rate of 71.5%. This discharge profile is composed of two plateaus, at 2.3V and 2.1V, respectively. As explained earlier, the 2.3V plateau corresponds to reactions that convert elemental sulfur to long-chained, soluble lithium polysulfides. On the other hand, the 2.1V corresponds to the reactions that reduce these polysulfides all the way to Li_2S_2 and Li_2S, which are insoluble in the organic solvents. As current rate increases, both the discharge capacity and charge capacity decrease, a common phenomenon for all kinds of lithium

batteries. Also, the voltage difference in charge and discharge profiles gets wider with an increasing current rate. It shows that an extra potential difference (or overpotential) is needed to drive the current flow at high current rate. At a high current rate of 560 mA/g, the discharge capacity is still over 800 mAh/g, showing good conductivity of the composite material that allows fast kinetics of the battery at this current rate.
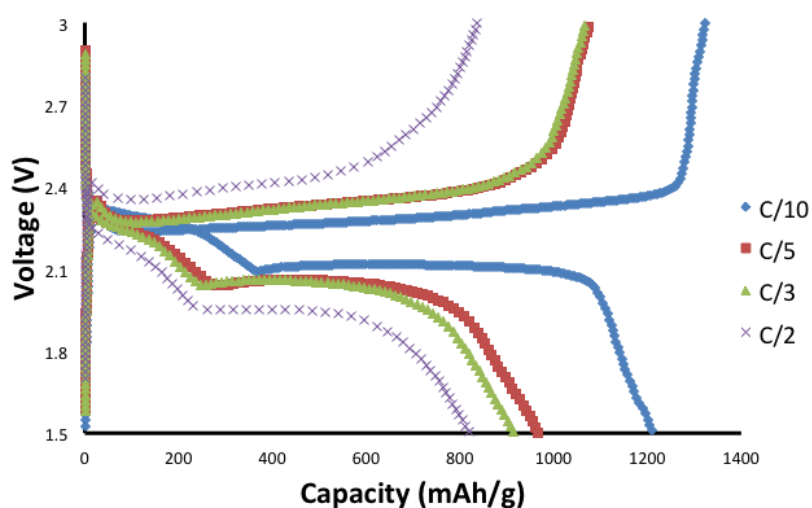
Figure 2-6. Battery performance of HPC-S80 tested at different current rates.
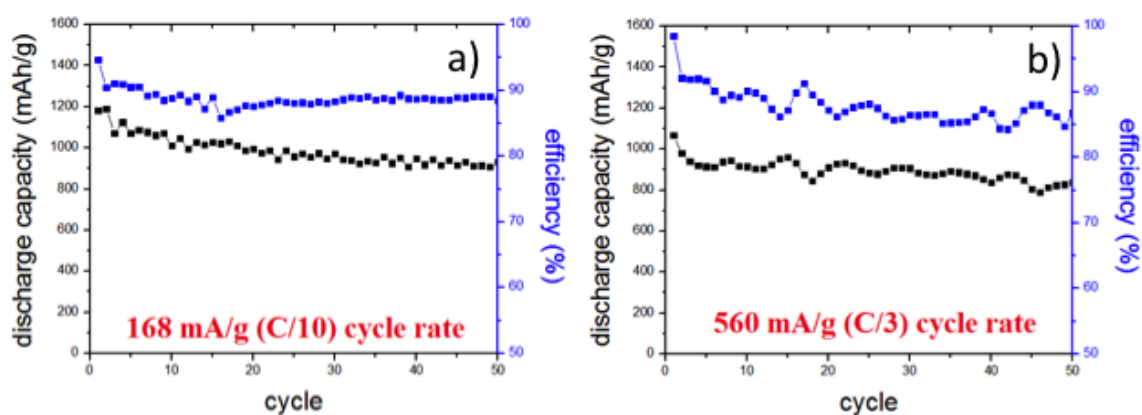
Figure 2-7. Battery cycling performance of HPC-S80 material at a) C/10 and b) C/3 current rate.

Figure 2-7 shows cycling testing results of the HPC-S80 material at a) C/10 current rate and b) C/3 current rate. At the lower rate of C/10, the starting discharge capacity was 1184 mAh/g while the discharge capacity decreased to 931 mAh/g at the 50th cycle, representing retention of 78.6% for the first 50 cycles. At the higher rate of C/3, the discharge capacity decreased from 1066 mAh/g for the 1st cycle to 837 mAh/g for the 50th cycle, representing similar retention of 78.5%. The discharge capacity at C/3 fluctuated severely over cycles, mostly because of the temperature change around the clock. On the other hand, the discharge capacity at C/10 was more stable over cycles because it took longer time to finish a cycle and the temperature fluctuation was evened off during that time. (For such discharge capacity at C/10, it takes ~6 hours to discharge and ~12 hours to finish a cycle. That is why we can observe in part of the plot a periodicity of 2 cycles, which is close to 24 hours, or a day.) At both rates, the columbic efficiency was between 85% and 90%. The high columbic efficiency indicates good absorption effect on the lithium polysulfides by the porous carbon and that the shuttle phenomenon was not severe.

When compared with the results in reference using CMK-3–sulfur composite,[1] our results evidently shows the advantage of using HPC as sulfur host (**Figure 2-8**). Although the two C/S composites in both reports showed similar retention of capacity, the HPC-S80 composite afforded higher discharge capacity than that of CMK-3-S70 composite, where the discharge capacity is calculated based on the mass of sulfur. Moreover, when we calculate the discharge capacity based on the mass of C/S composite, which is more useful in practice, the benefit of using HPC-S80 over CMK-3-S70 is even greater. HPC-S80 contains 80w% of sulfur while CMK-3-S70 contains 70w% of sulfur. The difference in capacity based on C/S composite if even greater than that is based on sulfur. In addition, as material cost is concerned, when switching from CMK-3-S70 to HPC-S80, 10w% of expensive synthetic carbon is replaced by cheap sulfur.
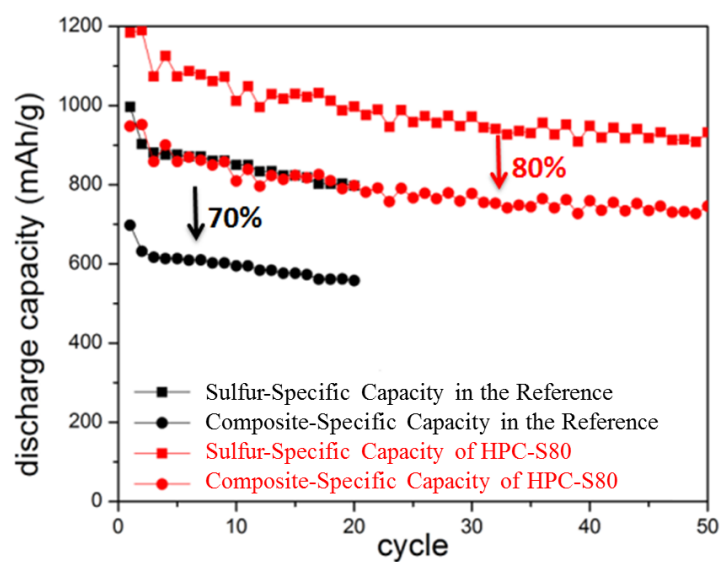
Figure 2-8. Comparison of battery cycling performance at C/10 between HPC-S80 and CMK-3-sulfur composite with 70% sulfur content.

2.4 Conclusion

HPC carbon material was designed and synthesized to have high pore volume and surface area for applications in lithium-sulfur batteries. Both pore volume and surface area are critical for the battery performance of porous carbon-sulfur composites. In particular, it was found that, porous carbon with a high pore volume can allow satisfactory battery performance of its sulfur composite with higher sulfur content, which is necessary for the development of high-energy Li-S battery. This way, the energy density of the battery can be increased, but at a lower cost because of less amount of synthetic carbon used. The best battery cycling performance of carbon-sulfur composites may not be obtained at the lowest sulfur content, because diffusion loss of polysulfides may be severe at low sulfur contents. The best performance may be obtained when majority of the pore volume of carbon is occupied by sulfur, example HPC-S70 or HPC-S80 in this case. At current rate of C/10, HPC-S80 demonstrated a high reversible capacity above 800 mAh/g after 50 cycles. The high reversible capacity and high sulfur content in the cathode material would yield a much higher energy density for Li-S batteries compared with previously reported designs of carbon-sulfur composites.

Reference (Chapter 2)

[1]   X. Ji, K. T. Lee, L. F. Nazar, *Nat. Mater.* **2009**, *8*, 500–506.

[2]   C. Liang, N. J. Dudney, J. Y. Howe, *Chem. Mater.* **2009**, *21*, 4724–4730.

[3]   S. Xin, L. Gu, N.-H. Zhao, Y.-X. Yin, L.-J. Zhou, Y.-G. Guo, L.-J. Wan, *J. Am. Chem. Soc.* **2012**, *134*, 18510–18513.

[4]   R. Elazari, G. Salitra, A. Garsuch, A. Panchenko, D. Aurbach, *Advanced Materials* **2011**, *23*, 5641–5644.

[5]   L. Ji, M. Rao, S. Aloni, L. Wang, E. J. Cairns, Y. Zhang, *Energy. Environ. Sci.* **2011**, *4*, 5053.

[6]   M. Rao, X. Song, E. J. Cairns, *J. Power Sources* **2012**, *205*, 474–478.

[7]   J. Schuster, G. He, B. Mandlmeier, T. Yim, K. T. Lee, T. Bein, L. F. Nazar, *Angew. Chem.* **2012**, *51*, 3591–3595.

[8]   C. Wang, J. Chen, Y. Shi, M. Zheng, Q. Dong, *Electrochim. Acta* **2010**, *55*, 7010–7015.

[9]   S. Wei, H. Zhang, Y. Huang, W. Wang, Y. Xia, Z. Yu, *Energy. Environ. Sci.* **2011**, *4*, 736.

[10]   R. Liu, Y. Shi, Y. Wan, Y. Meng, F. Zhang, D. Gu, Z. Chen, B. Tu, D. Zhao, *J. Am. Chem. Soc.* **2006**, *128*, 11652–11662.

[11]   C. J. Brinker, Y. F. Lu, A. Sellinger, H. Y. Fan, *Advanced Materials* **1999**, *11*, 579–585.

Chapter 3

Nanostructured Carbon-Sulfur Composite Microspheres with High Tap Density to Enable High-Areal-Capacity Cathodes for Practical Applications

3.1 Introduction

Despite its high theoretical energy density and high specific capacity,[1,2] the fledging technology and Li-S batteries still faces radical challenges. The low achievable capacity and capacity decay are attributed to two inherent properties of the battery system, namely the low electric conductivity of sulfur and the dissolution of polysulfides in the electrolyte.[3–9]. Among the diverse approaches explored to address these challenges, nanostructured carbon-sulfur composites have been proved to successfully increase and stabilize the achievable capacity.[10–13] Well-designed porous carbon frameworks can confine sulfur particles at the nanoscale, serving to address both of the core challenges of Li-S batteries. Such frameworks provide a highly-conducting network for electron transfer, thus enabling faster lithiation/delithiation process and improving sulfur utilization. In addition, their high surface area can trap polysulfides in the cathode through physical adsorption and thus improve capacity retention during cycling.

This chapter explores suitable material designs for Li-S batteries in practical applications. Although the sulfur-specific capacity and capacity retention are two key parameters to evaluate its potential as the next-generation battery chemistry, several other factors are also critical for the development of high-energy Li-S batteries but have received little attention in the literature – in particular, these include 1) tap density of cathode materials, 2) sulfur content in cathode materials, and 3) sulfur loading of electrodes. The tap density of a cathode material plays a key

role in determining its volumetric capacity – a higher tap density indicates denser packing of the cathode material, and thus higher volumetric capacity.[14] Much of the work to date on sulfur cathodes has focused on cathode materials with sub-micron-sized or nano-sized particles; however, it is well known that such small particles generally exhibit a relatively low tap density. Sulfur content (mass fraction of sulfur in cathode materials) affects the specific capacity of the cathode material as a whole, which is simply the multiplication product of sulfur-specific capacity and sulfur content. However, increasing the sulfur content can make it difficult to maintain good overall ionic and electrical conductivities and suppress the polysulfide shuttle, leading to decreased sulfur-specific capacity and poorer cycling stability and rate performance.[15] Finally, sulfur loading of electrodes (amount of sulfur coated on electrodes) determines the total capacity per electrode, and consequently the energy density of a battery. Electrodes with high sulfur loading – and thus with high capacity – are required for fabricating high energy density batteries, as they decrease the relative content of inactive components in the battery, such as current collectors and membranes.[16–18] Assuming a discharge voltage of 2V and specific capacity of 800 mAh g^{-1} for Li-S cathodes, a sulfur loading of 5 mg-S cm^{-2} is necessary to get an energy density comparable with that of cathodes in commercial LIBs (see calculation in Experimental Section). However, achieving such a high sulfur loading in electrodes is difficult with conventional Li-S cathode materials, as their sub-micron-sized or nano-sized particles lead to severe cracking of the electrode with increased loading; previous publications mostly reported electrode loadings of only 1-2 mg-S cm^{-2} when using industry-adopted coating techniques.[11,13,19–23] In addition, high loading can lead to increased electrical and ionic resistance and thus poor rate performance.[15] These three parameters need to be optimized, but raising each can be detrimental to capacity and rate performance. The key to balancing these competing parameters is the design of high-performance, well-optimized cathode materials.

Micro-sized materials have favorable properties in Li-S battery applications compared with sub-micron-sized or nano-sized materials. Such materials generally possess a higher tap density, granting them higher volumetric energy density. They also have a lower number of particle-particle interfaces, often leading to a lower contact resistance and easier-to-bind electrodes. Combining these advantages of micro-sized materials with the aforementioned advantages of nanostructured carbon-sulfur composite, here we report the design of a carbon framework that possesses both micro-sized spherical particle morphology and hierarchical mesopores to form a porous spherical carbon-sulfur composite (PSC-S). Both microscale particle morphology and pore structure in the porous spherical carbon (PSC) were well controlled by combining emulsion polymerization and evaporation-induced self assembly (EISA) process. PSC-S composite boasts a high tap density of 1.08 g ml^{-1} and contains 75 wt.% sulfur embedded into the mesopores of its carbon framework. At a high sulfur loading of 5 mg-S cm^{-2} and 60wt.% sulfur content in the electrode, this material delivers both high gravimetric and high volumetric capacity with excellent retention. Carbon nanotubes (CNTs) can also be readily incorporated into the microspherical structure in the synthesis process to form a porous spherical carbon-carbon nanotube-sulfur composite (PSC-CNT-S). CNT incorporation effectively raises the conductivity of the composite, and thus significantly improves its high-rate performance. At a high current density of 2.8 mA cm^{-2}, an initial capacity of 1100 mAh g^{-1} and a reversible capacity of 700 mAh g^{-1} after 200 cycles were achieved in PSC-CNT-S. The resultant areal capacity of over 3.5 mAh cm^{-2} is much higher than in previous reports of Li-S cathodes fabricated using coating techniques.

3.2 Experimental section and characterization methods

Materials: block copolymer F127 (Mw=12600, $PEO_{106}PPO_{70}PEO_{106}$), tetraethyl orthosilicate (TEOS, 99%), Span 80 (viscosity 1200-2000 mPa.s at 20^oC), Multiwalled carbon nanotube (CNT, OD*L, 6-9 nm*5 μm) were purchased from Sigma-Aldrich. Ethanol (> 99.8%), hydrochoric acid (HCl, 36.5 %), hydrofluoric acid (HF, 48~51%), carbon disulfide (CS_2, 99.8%), Triton X-100 were purchased from Alfa Aesar. Paraffin oil (light) was purchased from EMB Millipore. Colloidal silica latex SNOWTEX ST-O (10-20 nm, 20 wt.%) was gifted by Nissan Chemical America Corporation. The resin precursor (Mw <500) was prepared according to the literature method.[27]

Synthesis of PSC microspheres: In a typical preparation of PSC, 3.3g F127 was first dissolved in 20g ethanol with 2.0g HCl (0.2 M). Then, 4.16 g TEOS was added and the clear solution was stirred for 0.5h at 40°C. Next, 11g resin solution (20 wt.%) and 12 ml of colloidal silica ST-0 were added in sequence and further stirred for 1 h. Meanwhile, 3g of emulsifier, Span80, was dispersed in a 300 ml paraffin oil bath at 40°C. The ethanol solution was added into the oil bath for emulsification by vigorous stirring. The temperature was kept at 40 °C for 1 h and tuned to 100 °C to evaporate ethanol and thermopolymerize overnight. The as-made products were filtered and washed with hexane for several times before drying in air. Calcination was carried out sequentially in a tubular furnace, first at 350 °C for 3 h and next at 900 °C for 2 h under Ar flow to get $PSC-SiO_2$ nanocomposite. The heating rate was 1 °C/min below 600 °C and 5 °C/min above 600 °C. The $PSC-SiO_2$ nanocomposite was immersed in 2 wt.% HF solutions to remove silica, leaving PSC carbon spheres. The as-made product was washed by distilled water several times and dried at 80 °C in an oven.

Synthesis of PSC-CNT microspheres: PSC-CNT was synthesized similarly. 200 mg CNTs was dispersed in 20 ml ethanol with the assitance of Triton X-100 and sonication. This suspension was added to the ethanol solution of resin, F127, TOES, ST-0, and HCl and stirred for 0.5h before being emulsified in the paraffin oil bath.

Synthesis of PSC-S and PSC-CNT-S composites: To synthesize the PSC-S and PSC-CNT-S composites, 750mg sulfur was first dissolved in CS_2 by stirring. 250mg of PSC or PSC-CNT was then added to the solution and allow CS_2 evaporation under stirring. The mixture was then transferred into a closed bottle and heated at 155°C for 8 hours to yield the sulfur-embedded composites.

Electrochemical measurement: The electrochemical experiments were performed using 2016-type coin cells, which were assembled in an argon-filled dry glovebox (MBraun, Inc.) with the PSC-S, PSC-CNT-S, and SuperP-S electrodes as the working electrode and the Li metal as the counter electrode. The PSC-S and PSC-CNT-S electrodes were prepared by casting the slurry consisting of 80 wt.% of either carbon-sulfur composite, 12 wt.% of Super P carbon black, and 8 wt.% of polyvinylidene fluoride (PVDF) binder. The SuperP-S electrodes were prepared by casting the slurry consisting of 92 wt.% of sulfur/super P ball-milled mixture and 8 wt.% of polyvinylidene fluoride (PVDF) binder, where the sulfur-super P mixture was ball milled overnight at a speed of 500 rpm. All electrodes have a loading of 5.0 mg-S cm^{-2} (±5%) by controlling the area of coating. 1 M LiTFSI and 0.2 M $LiNO_3$ in a mixture of 1,3-Dioxanes and Dimethoxyethane (DOL: DME, 1:1 by vol.%) was used as the electrolyte (Novolyte Technologies, Independence, OH). The electrochemical performance was evaluated by galvanostatic charge/discharge cycling on an Arbin BT-2000 battery tester at room temperature

under different current densities in the voltage range between 1.7 and 2.8 V versus Li+/ Li. The specific capacity are calculated based on the mass of sulfur.[37,38]

Characterization: The crystalline structure of the as-prepared composite was characterized by X-ray diffraction (XRD) on a Rigaku Miniflex II spectrometer. The microstructure of the composite particles were investigated with a JEOL 1200 transmission electron microscope (TEM). Scanning electron microscope (SEM) was one on a LEO 1530. The surface area and pore structure were characterized by nitrogen sorption using a Micrometrics ASAP 2020 physisorption analyzer. The surface area was calculated by the Brunauer–Emmett–Teller (BET) method. The pore size distributions were derived from the adsorption branches of isotherms using the Barrett–Joyner–Halenda (BJH) model. The content of sulfur in the composites was characterized by thermogravimetric analysis (TGA) in the temperature range of 25-600°C with a heating rate of 10°C min^{-1} under nitrogen atmosphere. Dynamic light scattering (DLS) experiments were performed on a Malvin Mastersizer. Electrical resistivity of powder materials were measured by compressing the powder in a cylindrical space and getting its resistance, which is then converted to conductivity and resistivity using the geometrical parameters of the cylindrical space. The pressure among powder particles can be controlled with the force of compression.

Calculation for necessary sulfur loading of sulfur cathode: To reach a similar energy density to that of Li-ion batteries in pouch cell or cylindrical cell configuration, the energy per area for electrodes (or the energy loading, L_{en}) should be approximately the same. The energy loading of an electrode can be calculated this way:

$$L_{en} = V \times C \times L$$

where V is the average working voltage of the active material; C is the specific capacity of the active material; and L is the electrode loading of active material.

Take $LiCoO_2$ as a typical cathode active material for Li-ion batteries and 15 mg/cm2 as a typical electrode loading for this material, its corresponding energy loading is

$$L_{en,LiCoO_2} = V \times C \times L = 3.8V \times 150\frac{mAh}{g} \times 15\frac{mg}{cm^2} = 8.55\frac{mWh}{cm^2}$$

When using sulfur as the cathode active material, the average working voltage is about 2.1V. Practical retainable capacity is about 800 mAh/g. Under these conditions, the electrode loading needed to reach $L_{en,LiCoO_2}$ is

$$L = \frac{L_{en}}{V \times C} = \frac{8.55\frac{mWh}{cm^2}}{2.1V \times \frac{800mAh}{g}} = 5.09\frac{mg}{cm^2}$$

3.3 Results and discussion

3.3.1 Synthesis and characterization

The synthesis process of micro-sized PSC-S spheres is schematically illustrated in **Figure 3-1a**. In order to simultaneously control both the micro-scale morphology and mesoporous structure, a combined process of emulsion polymerization and EISA was adopted.[24–27] The emulsion polymerization process is known to facilitate formation of microspherical particles, while EISA can assemble building blocks of framework precursor and pore templates into homogeneous mesostructures through a facile solvent evaporation process. Briefly, carbon precursor (phenolic formaldehyde resin) and several pore templates, namely tetraethyl orthosilicate (TEOS), tri-block copolymer Pluronic F127 (F127), and silica colloids, were homogeneously mixed in ethanol under mild acidic and heating conditions for pre-hydrolyzation. The aforementioned precursor solution was emulsified in mineral oil by the emulsifier Span 80 under constant mechanical stirring. The emulsion was then heated to 100°C to allow ethanol evaporation and further polymerization of the resin. As the precursor concentration increased, the emulsion droplets underwent an EISA process to form micro-sized spheres containing self-assembled mesostructured building blocks. In the EISA process within the droplets, TEOS underwent hydrolysis and condensation process to form silicate. The silicate, F127, and silica colloids co-directed self-assembly of the resin oligomer into mesostructures via hydrogen bonding.[27] The use of multiple pore templates is to generate hierarchical mesoporous structures with both high surface area (to increase electrochemically active sites) and high pore volume (to increase available space for sulfur embedding). Meanwhile, the emulsifier Span 80 can prevent aggregation of these micro-sized droplets during thermal polymerization and thus preserve their

microspherical morphology. After carbonization and removal of templates, the hierarchical

mesoporous carbon microspheres were obtained and denoted as PSC.
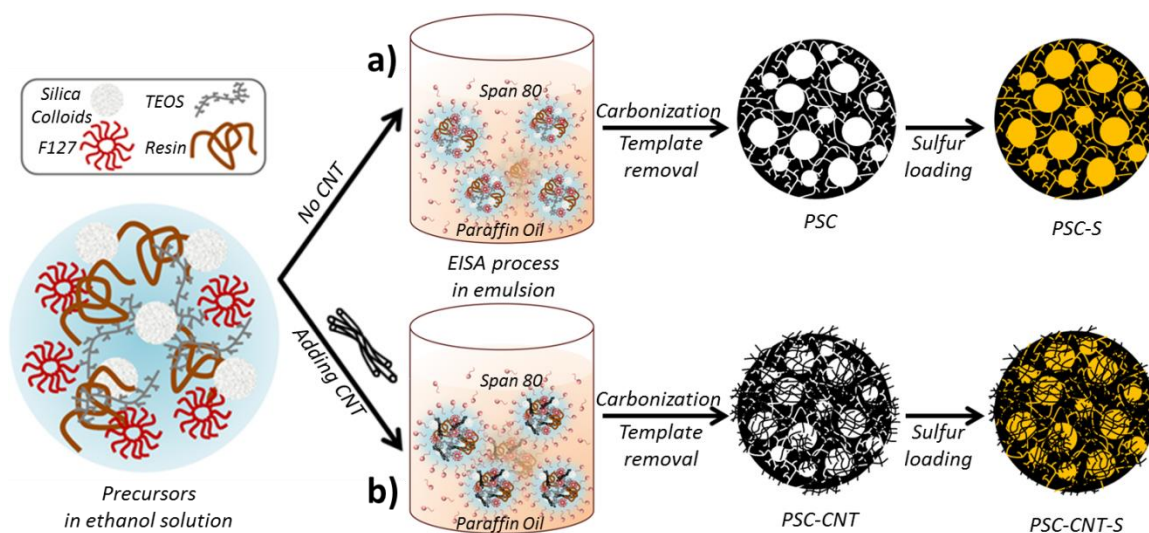
Figure 3-1. Schematic illustration for the synthesis of (a) PSC-S and (b) PSC-CNT-S using a combination of emulsion polymerization process and EISA method**.**

The micro-scale morphology of PSC particles was studied by scanning electron

microscopy (SEM). SEM images confirm that PSC takes the form of micro-sized spheres (**Figure 3-2a**). These spheres have smooth surfaces and diameters in a few tens of microns. The volume

median diameter of PSC particles was further confirmed by dynamic light scattering (DLS) to be

approximately 37μm (**Figure 3-2c**), with the 10th and the 90th percentile at 22μm and 63μm,

respectively. The micro-scale particle sizes of these materials are very suitable for fabricating

electrodes with high loading. On the other hand, ball-milling the PSC microspheres may result in

shattered particles with irregular shapes and a much reduced diameter (**Figure 3-3a**). These

particles resemble those synthesized without morphology control and may yield poor electrode

quality when used as electrode materials.

The nanostructure of PSC was investigated by transmission electron microscopy (TEM) and N_2 sorption analysis. TEM image (**Figure 3-2b**) reveals that PSC has a disordered porous structure. Its nitrogen sorption isotherm (**Figure 3-2d**) resembles a typical Type IV isotherm with H1 hysteresis, indicating mesoporous structure. The Barrett-Joyner-Halenda (BJH) pore size distribution (**Figure 3-2d inset**) derived from N_2 absorption shows a peak around 12 nm, with the majority of the mesopores ranging from 5 to 25 nm in diameter. It is known that the pore size is determined by the employed templates, including silica colloids (10-20 nm), F127 micelle (4-8 nm), and silica from hydrolyzation and condensation of TEOS (<3.5nm).[27] This BJH pore size distribution indicates the majority of mesopores are templated from silica colloids and F127. On the other hand, TEOS templates smaller mesopores in the carbon wall, which generates high surface area and prevents framework shrinkage during carbonization process. PSC has a high Brunauer-Emmet-Teller (BET) surface area of 1014 m^2 g^{-1} and a high BJH pore volume of 2.5 cm^3 g^{-1}, which are critical to battery performance.
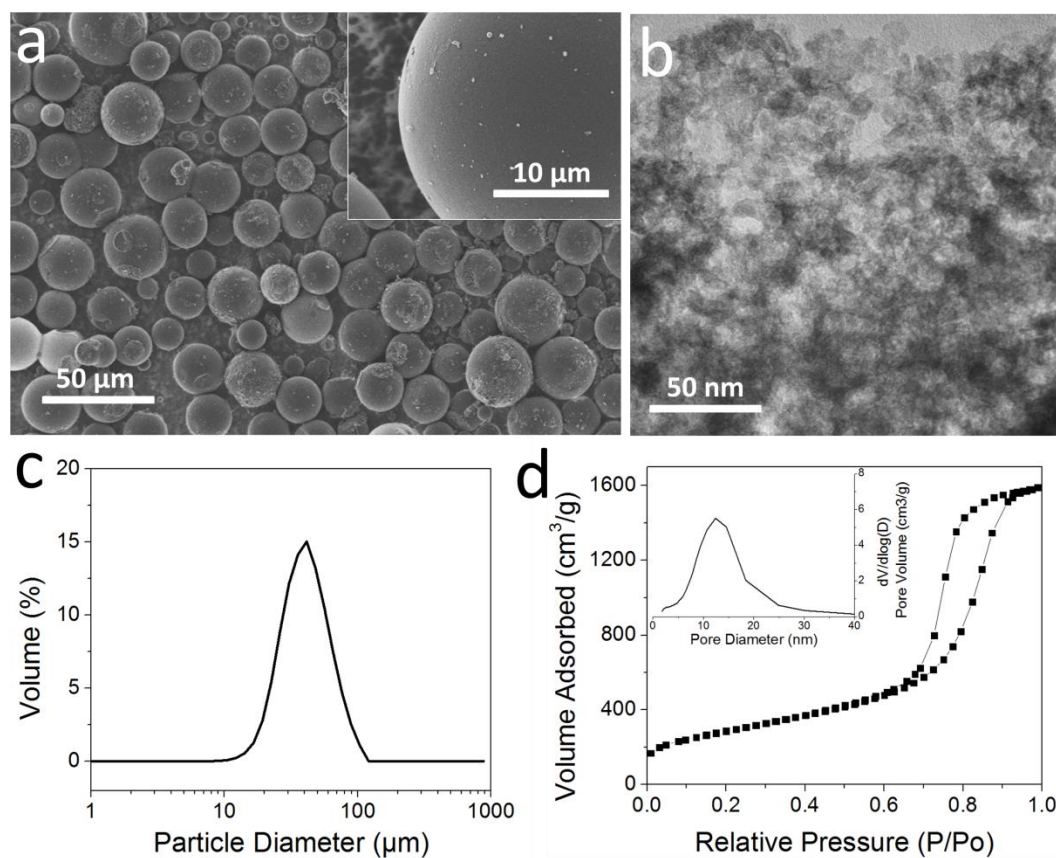
Figure 3-2. (a) SEM of PSC carbon microspheres; (b) TEM of PSC; (c) DLS measurement on PSC after dispersing particles in water; (d) N_2 sorption isotherms of PSC with inset showing pore size distributions.
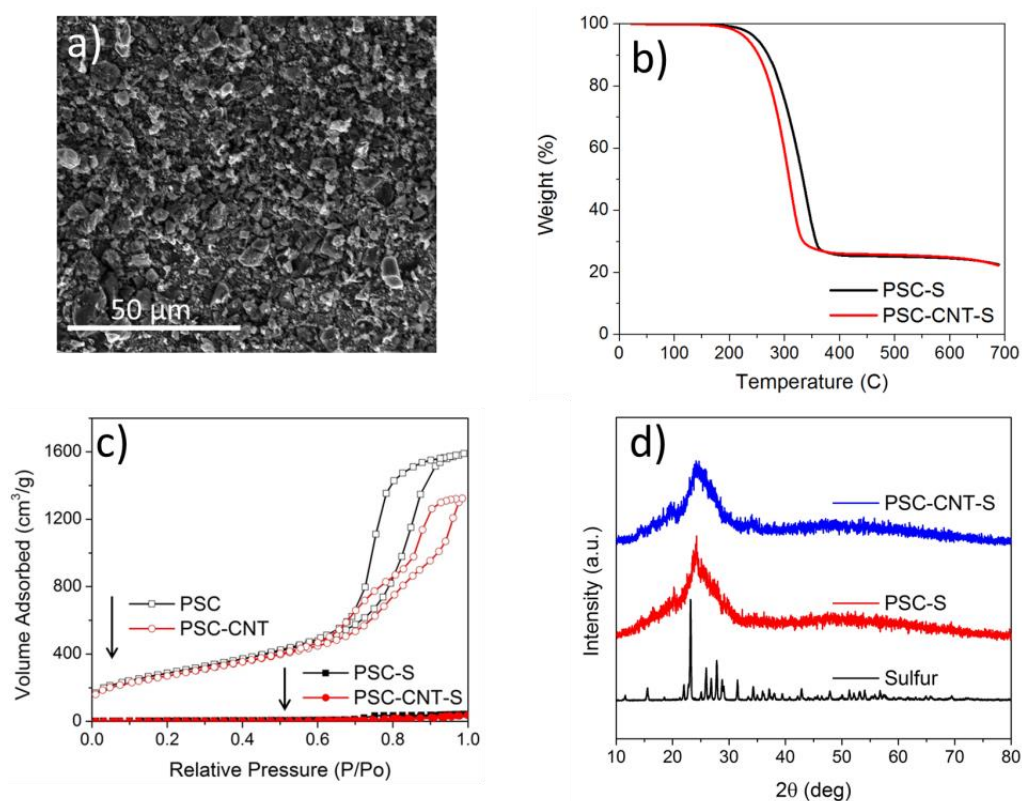
Figure 3-3. (a) SEM of PSC-bm carbon material; (b) TGA of PSC-S and PSC-CNT-S; (c) N_2 sorption isotherms of PSC and PSC-CNT before and after sulfur embedding; (d) X-ray diffraction (XRD) patterns of S, PSC-S, and PSC-CNT-S.

Table 3-1. Tap densities (mg ml^{-1}) of different carbon-sulfur composite materials

	PSC-S	PSC-bm-S	SuperP-S	PSC-CNT-S
Tap density	1.08	0.72	0.39	0.80

Sulfur was then embedded into PSC with a solvent diffusion method to form PSC-S composite.[28] Sulfur content in the composite was controlled at 75 wt.% and confirmed by thermogravimetric analysis (TGA) (**Figure 3-3b**). Nitrogen sorption measurements of the composite (**Figure 3-3c**) shows negligible pore volume remaining after sulfur embedding, confirming that sulfur occupies the pores of the carbon framework. X-ray diffraction (XRD) pattern of the composite (**Figure 3-3d**) shows no pronounced peaks associated with bulk sulfur, further indicating that sulfur is confined into the mesopores of the carbon frameworks. Owing to its micro-sized spherical shape in design, PSC-S exhibit an extremely high tap density of 1.08 g ml^{-1}, compared with the intrinsic density of ~2.0 g ml^{-1} for both amorphous carbon and sulfur (**Table 3-1**). The corresponding particle packing density is ~54%, approaching the density of 74% for close packing of mono-sized spheres and 64% for random close packing of mono-sized spheres.[29] This discrepency in packing density between the achieved and theoretical value can be attributed to the size variation, the porous structure, and the relatively loose packing of particles. In contrast, by breaking down PSC-S into much smaller and irregular pieces, PSC-bm-S showed a tremendous drop in tap density to 0.72 g ml^{-1}. Super P-sulfur composite (SuperP-S), prepared by mixing commercial carbon Super P and sulfur with the same sulfur content, has an even lower tap density of 0.39 g ml^{-1}. A higher tap denisty of battery material is desired for higher volumetric energy density.

3.3.2 Battery testing

PSC-S was evaluated as a cathode material for Li-S batteries by galvanostatic charging/discharging in a coin-cell configuration with lithium metal as the anode. The electrodes were fabricated by doctor blade coating using C-S composite, Super P, and PVDF binder with a ratio of 80:12:8. The sulfur content in the cathode was thus 60 wt.%. The thickness of the electrodes was carefully controlled to get an electrode loading of around 5 mg-S cm^{-2}. SuperP-S electrodes with the same sulfur content and electrode loading were used as control samples. The coating quality of electrodes were shown in **Figure 3-4**. Because of the ideal particle sizes and high tap density of PSC-S material, its resultant electrode was very smooth and visually crack-free. On the other hand, PSC-bm-S electrode showed severe cracking due to the significant decrease in particle sizes and tap density. The SuperP-S electrode showed even worse cracking and visible peeling. Electrodes with poor coating quality like the latter two are not viable for battery fabrication, as loose particles may easily come off of the current colletor and form short circuits in a cell structure and fail the battery.
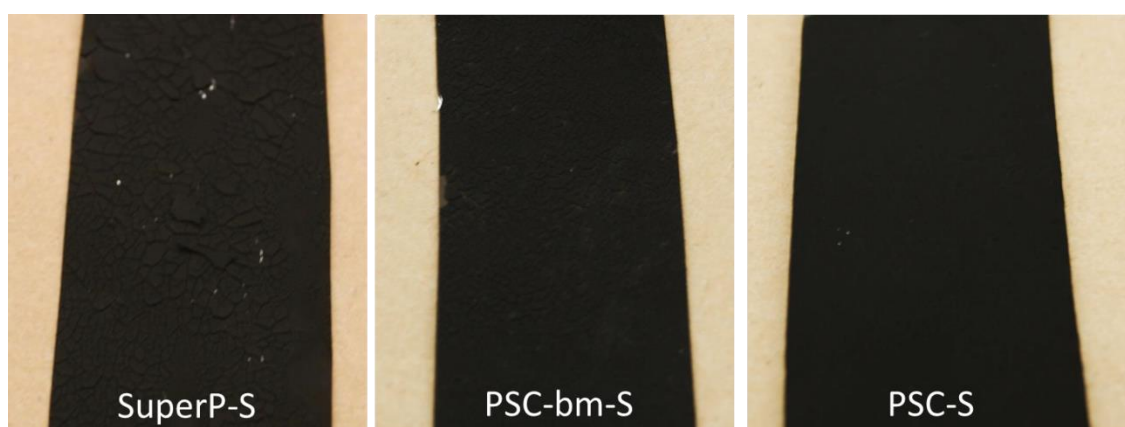
Figure 3-4. photo images of electrodes using three different cathode materials.

To verify the impact of sulfur loading on battery performance, SuperP-S composite (the mixture of 75wt.% sulfur and 25wt.% Super P) was used to form electrodes with different sulfur loading and tested in batteries. The cycling performance of this material with two sulfur loading was shown in **Figure 3-5**. The current rates for both batteries are C/10, or 168mA/g, but the actual currents are different by a factor of 10 due to the difference in sulfur loading of electrodes. The electrode with higher sulfur loading showed much lower capacity (or utilization rate) and retention. The poor performance with high sulfur loading can be attributed to the following: 1) the resulting high current is challenging for the conductivity of the electrodes and the reaction kinetics; 2) electrolyte saturation in the electrolyte may be difficult; 3) passivation of electrodes may be more severe.
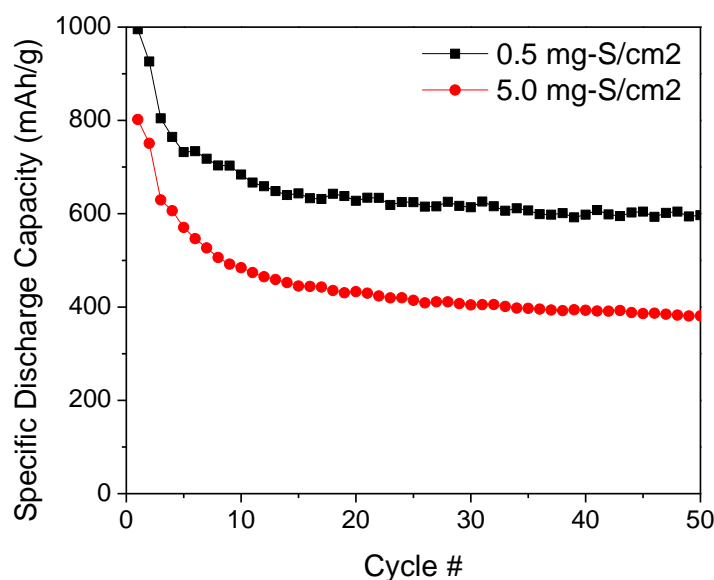
Figure 3-5. Discharge capacity over cycles using the same cathode material of SuperP-S, but with different sulfur loading. The current rate is C/10. (Note that the actual currents for the two batteries are different due to the difference in mass of sulfur.)

Electrodes of PSC-S composite showed much improved battery performance on electrodes with high sulfur loading (5 mg-S/cm^2). The initial sulfur-specific discharge capacity reached ~1150 mA h g^{-1} during activation using a low current density of 0.42mA cm^{-2} (**Figure 3-6**a). This initial capacity is close to 70% of the theoretical capacity, showing high utilization of sulfur, likely owing to the intimate contact between nano-sized sulfur particles and the mesoporous carbon framework. Cycling continued at 0.84 mA cm^{-2} after the initial two activation cycles, and the capacity of PSC-S stabilized at around 800 mA h g^{-1} within the subsequent three cycles. A reversible capacity of 740 mA h g^{-1} was still delivered after 50 cycles, showing ~91% capacity retention after the first stable cycle, an average drop of 0.20% per cycle. The major capacity drop in the first 5 cycles, a behavior commonly observed in Li-S batteries, may be due to diffusion loss of sulfur species and irreversible formation of Li$_2$S. It is recognized that increased sulfur loading generally leads to significantly decreased specific capacity.[15] The capacity of the PSC-S composite electrodes is thus impressively high given their high sulfur loading. The high reversible capacity can be attributed to the synergetic effect of several features of PSC-S, namely its high surface area for polysulfide adsorption, intimate contact between carbon and sulfur, and better mechanical integrity of the electrode that prevents structural collapse due to its micro-sized, rigid framework. In contrast, SuperP-S delivered much lower capacity and showed fast capacity fading, due to its large sulfur particle size, ease of polysulfide diffusion loss, and loose framework. Moreover, calculated as the multiplication product of tap density and gravimetric capacity, the volumetric capacity of PSC-S is much higher than that of SuperP-S because of their difference in tap density (**Figure 3-6b**).[30,31] At the end of 50 cycles, PSC-S outperformed Super P-S in volumetric capacity by a factor of 5.

As previously discussed, electrode loading has a significant impact on the energy density of a battery, as higher-loading electrodes mean a lower content of inactive components (such as

current collectors and separators) needed for a target cell-level energy density. Previous reports have often used low electrode loading (<2 mg-S cm^{-2}) when using industry-adopted coating techniques, whereas we have determined that an electrode loading of at least 5 mg-S cm^{-2} (i.e. an areal capacity of 4 mAh cm^{-2} assuming 800 mAh g^{-1} specific capacity) is necessary to achieve similar energy density to LIB cathodes at the electrode level. Plotted in **Figure 3-6c**, the resultant areal capacity of PSC-S at 50th cycle is much higher than that of previous reports, and close to our target value at 4 mAh cm^{-2}.
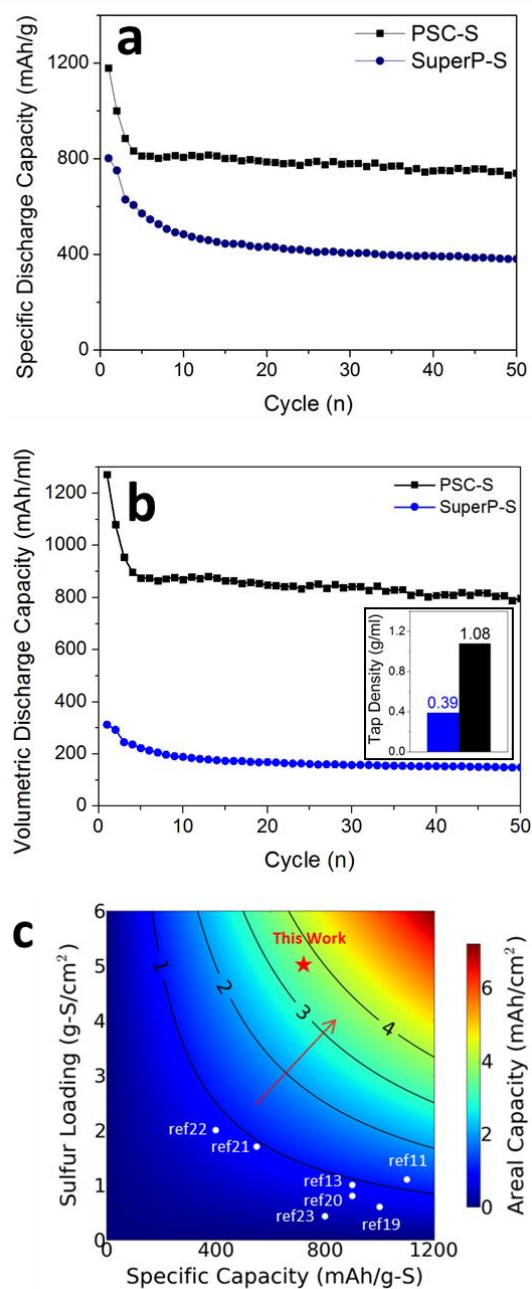
Figure 3-6. Comparison of cycling performance between PSC-S and SuperP-S at 0.84 mA cm-2 read in (a) specific discharge capacity and (b) volumetric discharge capacity with the inset showing tap density of the two materials; (c) comparison of areal capacity in this work with those in the references at 50th cycle (or the last cycle if cycling ended before 50th cycle).

3.3.3 Performance enhancement by CNTs

High electrical resistance of the sulfur cathodes has long been attributed to limiting sulfur utilization and rate performance of Li-S batteries.[32,33] It gets even more challenging to maintain facile electron transfer with an increased sulfur loading in electrodes. Thus, we leveraged another strength of this synthesis approach, the easiness to incorporate additives into the carbon-sulfur composite, in order to decrease the electrical resistivity of the material and improve the rate performance of battery. CNTs were illustratively added to the system as conductivity enhancers to form PSC-CNT and PSC-CNT-S, with the latter showing much improved battery performance at high current densities compared with its CNT-free conterpart. PSC-CNT was synthesized similar to PSC, with the additional step of dispersing CNTs in the ethanol precursor solution by sonication and surfactant (Figure 1b, details in Experimental Section). The mass fraction of CNTs in PSC-CNT is estimated to be ~10%. SEM confirmed the micro-sized spherical morphology of PSC-CNT (**Figure 3-7a**). The particles have rougher surfaces and numerous protruding CNTs (**Figure 3-7a inset**). In addition, CNTs are well dispersed in the interior of the PSC-CNT particles (**Figure 3-7c** and **d**). Such a distribution of the conductive CNTs is highly desired to decrease both inter-particle and intra-particle electrical resistance and improve the electrode-level conductivity. The size distribution of PSC-CNT particles confirmed by DLS (Figure **Figure 3-7e**) is similar to that of PSC, with the volume median diameter to be 33μm. TEM images (**Figure 3-7b**) reveal a disordered mesoporous structure of PSC-CNT. CNTs can be found closely connected with the carbon framework in PSC-CNT. Nitrogen sorption measurement confirmed its mesoporous structure with Type IV isotherm (**Figure 3-7f**). The BJH pore size distribution plot for PSC-CNT shows a peak around 9nm, followed by a tail contributed by pores with larger sizes. The peak should represent pores templated by F127 and silica colloids; while the tail may represent some pore structures generated by the CNT network (visible in **Figure 3-7d**) or

aggregated templates. The BET surface area is 963 m^2 g^{-1} and the BJH pore volume is 2.1 cm^3 g^{-1}

for PSC-CNT. Both are slightly lower than those of PSC, mostly due to the ~10 wt.% CNT

content that has little pore structure. The PSC-CNT porous framework can also hold 75 wt.%

sulfur in its nano-sized pores (**Figure 3-4c and d**). The tap density of PSC-CNT-S is 0.80 g ml^{-1},

lower than that of PSC-S, which may be due to a looser structure with CNTs in the composite.
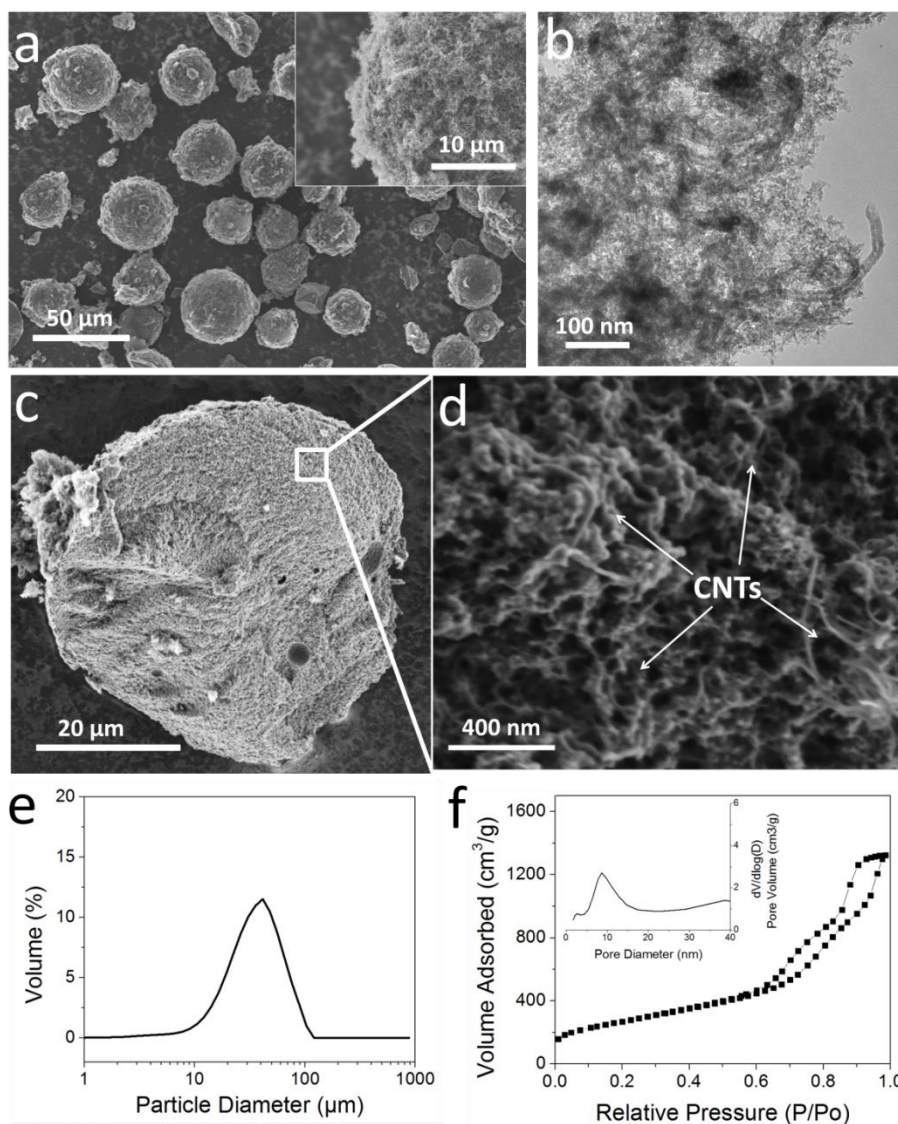
Figure 3-7. (a) SEM of PSC-CNT microspheres, inset shows a high-magnification image on the CNT protruding rough surface of the PSC-CNT microspheres; (b) TEM of PSC-CNT; (c) and (d) SEM of the cross-section on a fractured PSC-CNT microsphere; (e) DLS measurement of PSC-CNT after dispersing particles in water; (f) N_2 sorption isotherms of PSC-CNT with inset showing pore size distributions.
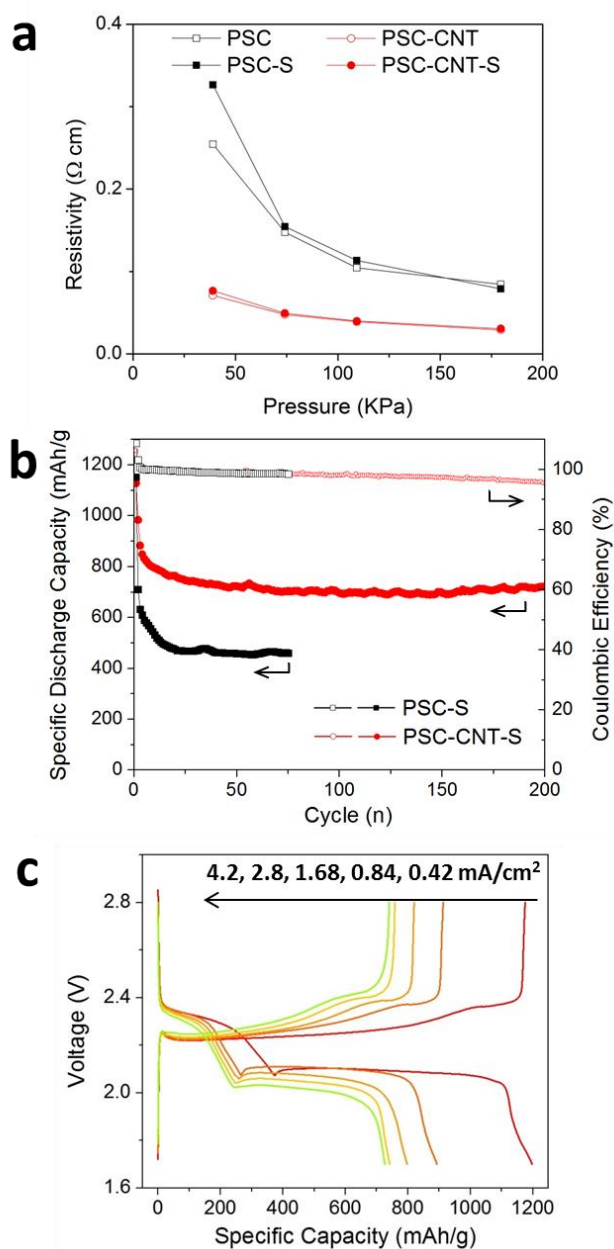
Figure 3-8. (a) Electrical resistivity and conductivity in the inset measured at various pressure; (b) comparison of cycling performance between PSC-CNT-S and PSC-S at 2.8 mA cm^{-2} with solid dots showing specific discharge capacity and hollow dots showing coulombic efficiency; (c) charge-discharge profiles of PSC-CNT-S at various current densities.

The electrical resistivity was measured at different pressures for PSC and PSC-CNT both before and after sulfur-embedding (**Figure 3-8**a). For all materials, the resistivity decreases with pressure as inter-particle contact improves. CNT incorporation causes a clear decrease in resistivity at all testing pressures. It's worth noting that neither PSC nor PSC-CNT exhibited a jump in resistivity after sulfur embedding. This indicates that sulfur is well confined in the pores instead of covering the outer surfaces of the particles, which would otherwise significantly increase contact resistance. This low sensibility of resistivity to sulfur embedding, as well as the resistivity values of these materials, are consistent with previous report.[11] PSC-CNT-S showed excellent battery performance at high current densities. As shown in **Figure 3-8b**, PSC-CNT-S exhibited stable cycling over 200 cycles at 2.8 mA cm^{-2}, which is an extremely high current density in battery applications.[15,34–36] (Note that the first two cycles are acivation cycles at 0.42 mA cm^{-2}.) The capacity remained above 700 mAh g^{-1}, showing ~87% capacity retention after the first stable cycle (5th cycle), an average drop of 0.067% per cycle. The coulombic efficiency kept around 98% and slowly dropped to 95% after 200 cycles, due to gradual consumption of LiNO$_3$ additive. In contrast, because of its lower conductivity and thus lower utilization of sulfur, PSC-S showed a lower specific capacity at this high current rate. The charge-discharge profiles of PSC-CNT-S at various current densities were shown in **Figure 3-8c**. As current density ramps up, both discharge capacity and output voltage showed mild decrease. However, due to the high conductivity of the material, neither capacity nor voltage profiles was severely affected.

3.4 Conclusion

Micro-sized spherical carbon-sulfur composites were designed to reach high tap density and high sulfur content, and to fabricate electrodes with high sulfur loading, with an eye toward practical applications of Li-S batteries. Both micro-spherical particle morphology and hierarchical mesoporous structure with high surface area and pore volume of the carbon frameworks were well controlled by a combination of EISA and emulsion polymerization. The carbon-sulfur composites had a high tap density of ~1 g ml^{-1} and were shown to have solid performance as Li-S cathodes despite the high electrode-level sulfur content of 60 wt.% and high sulfur loading of 5 mg-S cm^{-2} in electrodes. In addition, the incorporation of CNTs into the micro-spherical particles was found to decrease resistance of the composite, and allow for improved high-current-density performance. This highly scalable synthesis approach shows a promising direction for future designs of C-S composites as Li-S cathode materials for practical applications.

Reference (Chapter 3)

[1]   P. G. Bruce, S. A. Freunberger, L. J. Hardwick, J. M. Tarascon, *Nat. Mater.* **2012**, *11*, 19.

[2]   X. Ji, L. F. Nazar, *J. Mater. Chem.* **2010**, *20*, 9821.

[3]   J. Nelson, S. Misra, Y. Yang, A. Jackson, Y. Liu, H. Wang, H. Dai, J. C. Andrews, Y. Cui, M. F. Toney, *J. Am. Chem. Soc.* **2012**, *134*, 6337.

[4]   S. E. Cheon, K. S. Ko, J. H. Cho, S. W. Kim, E. Y. Chin, H. T. Kim, *J. Electrochem. Soc.* **2003**, *150*, A796.

[5]   C. Barchasz, F. Molton, C. Duboc, J. C. Leprêtre, S. Patoux, F. Alloin, *Anal. Chem.* **2012**, *84*, 3973.

[6]   Y. Diao, K. Xie, S. Xiong, X. Hong, *J. Power Sources* **2013**, *235*, 181.

[7]   N. A. Cañas, S. Wolf, N. Wagner, K. A. Friedrich, *J. Power Sources* **2013**, *226*, 313.

[8]   Y. Diao, K. Xie, S. Xiong, X. Hong, *J. Electrochem. Soc.* **2012**, *159*, A421.

[9]   Y. V Mikhaylik, J. R. Akridge, *J. Electrochem. Soc.* **2004**, *151*, A1969.

[10]   R. Elazari, G. Salitra, A. Garsuch, A. Panchenko, D. Aurbach, *Adv. Mater.* **2011**, *23*, 5641.

[11]   X. Ji, K. T. Lee, L. F. Nazar, *Nat. Mater.* **2009**, *8*, 500.

[12]   C. Liang, N. J. Dudney, J. Y. Howe, *Chem. Mater.* **2009**, *21*, 4724.

[13]   S. Xin, L. Gu, N.H. Zhao, Y. X. Yin, L. J. Zhou, Y. G. Guo, L. J. Wan, *J. Am. Chem. Soc.* **2012**, *134*, 18510.

[14]   Z. Chen, J. R. Dahn, *J. Electrochem. Soc.* **2002**, *149*, A1184.

[15]   S. E. Cheon, K. S. Ko, J. H. Cho, S. W. Kim, E. Y. Chin, H. T. Kim, *J. Electrochem. Soc.* **2003**, *150*, A800.

[16]   H. Zheng, J. Li, X. Song, G. Liu, V. S. Battaglia, *Electrochim. Acta* **2012**, *71*, 258.

[17]   C. J. Bae, C. K. Erdonmez, J. W. Halloran, Y. M. Chiang, *Adv. Mater.* **2013**, *25*, 1254.

[18]   S. S. Zhang, *J. Power Sources* **2013**, *231*, 153.

[19]   Z. W. Seh, W. Li, J. J. Cha, G. Zheng, Y. Yang, M. T. McDowell, P. C. Hsu, Y. Cui, *Nat. Commun.* **2013**, *4*, 1331.

[20]   J. Schuster, G. He, B. Mandlmeier, T. Yim, K. T. Lee, T. Bein, L. F. Nazar, *Angew. Chem. Int. Ed.* **2012**, *51*, 3591.

[21]   H. Wang, Y. Yang, Y. Liang, J. T. Robinson, Y. Li, A. Jackson, Y. Cui, H. Dai, *Nano Lett.* **2011**, *11*, 2644.

[22]   Y. M. Lee, N. S. Choi, J. H. Park, J. K. Park, *J. Power Sources* **2003**, *119*, 964.

[23]   Y. Yang, G. Yu, J. Cha, H. Wu, *Acs Nano* **2011**, *5*, 9187.

[24]   W. D. Harkins, *J. Am. Chem. Soc.* **1947**, *69*, 1428.

[25]   C. J. Brinker, Y. F. Lu, A. Sellinger, H. Y. Fan, *Adv. Mater.* **1999**, *11*, 579.

[26]   D. Gu, H. Bongard, Y. Deng, D. Feng, Z. Wu, Y. Fang, J. Mao, B. Tu, F. Schüth, D. Zhao, *Adv. Mater.* **2010**, *22*, 833.

[27]   R. Liu, Y. Shi, Y. Wan, Y. Meng, F. Zhang, D. Gu, Z. Chen, B. Tu, D. Zhao, *J. Am. Chem. Soc.* **2006**, *128*, 11652.

[28]   Y. Cao, X. Li, I. A. Aksay, J. Lemmon, Z. Nie, Z. Yang, J. Liu, *Phys. Chem. Chem. Phys.* **2011**, *13*, 7660.

[29]   G. D. Scott, D. M. Kilgour, *J. Phys. D: Appl. Phys.* **1969**, *2*, 863.

[30]   D. Applestone, A. Manthiram, *RSC Adv.* **2012**, *2*, 5411.

[31]   R. Yi, F. Dai, M. L. Gordin, S. Chen, D. Wang, *Adv. Energy Mater.* **2012**, 3, 295.

[32]   Y.S. Su, A. Manthiram, *Chem. Commun.* **2012**, *48*, 8817.

[33]   N. Jayaprakash, J. Shen, S. S. Moganty, A. Corona, L. A. Archer, *Angew. Chem. Int. Ed.* **2011**, *123*, 6026.

[34]   M. Hagen, S. Dörfler, P. Fanz, T. Berger, R. Speck, J. Tübke, H. Althues, M. J. Hoffmann, C. Scherr, S. Kaskel, *J. Power Sources* **2013**, *224*, 260.

[35]   N. Yabuuchi, T. Ohzuku, *J. Power Sources* **2003**, *119*, 171.

[36]   P. L. Taberna, S. Mitra, P. Poizot, P. Simon, J. M. Tarascon, *Nat. Mater.* **2006**, *5*, 567.

[37]   D. Pantea , H. Darmstadt , S. Kaliaguine , L. Summchen , C. Roy, *Carbon* **2001**, *39*, 1147.

[38]   D. Pantea , H. Darmstadt , S. Kaliaguine , C. Roy, *Appl. Surf. Sci.* **2006**, *217*, 181.

Chapter 4

Nitrogen-Doping Empowering Carbon Host with Chemical Adsorption of Both Sulfur and Polysulfides

4.1 Introduction

With its energy density 3-5 times that of lithium-ion batteries, the lithium-sulfur (Li-S) rechargeable battery is a promising candidate to take over as the next-generation energy storage device, urgently needed to sustain the quick expansion of our electrified society.[1-6] The abundance, low cost, and low toxicity of sulfur make this battery technology even more attractive and feasible for commercialization. Unfortunately, the attainable energy from such batteries currently is only a small fraction of the theoretical value.[7-14] Different from the successful lithium ion batteries based on intercalation mechanism, the Li-S battery has its active material dissolved and diffusing in the electrolyte in the form of polysulfides, which fails the complete reaction between sulfur and lithium. Li-S batteries operate by reaction of sulfur with lithium to sequentially form lithium polysulfides (i.e., Li_2S_x, $8 \geq x \geq 3$), lithium disulfide (Li_2S_2), and finally lithium sulfide (Li_2S) during the lithiation process, with the reverse occurring during the delithiation process. While S, Li_2S_2 and Li_2S have limited if any solubility in the electrolyte, polysulfides can readily dissolve into the electrolyte and consequently gives rise to a series of the challenges plaguing Li-S batteries. Firstly, polysulfides would diffuse and lose contact with the conductive network of the cathode, resulting in a continual loss of active material and consequently a low utilization rate and fast capacity decay. What's more, dissolved polysulfides would lose electrons to the lithium anode and retrieve electrons on the cathode while diffusing between electrodes, causing an internal short-circuit and suppressing charge efficiency at a low

level.[15] This behavior is termed polysulfide shuttle effect. Should the polysulfides be well confined in the cathode, Li-S batteries may well operate similar to Li-ion batteries and their complete energy may be unleashed.

This chapter introduces material designs to better trap polysulfides in the cathode. Researchers have tried many methods to achieve this goal. Conductive porous scaffolds possibly represent the most popular and successful solution to Li-S batteries. The scaffolds not only can effectively confine the particle size of sulfur and thus increase material utilization, the high surface area accompanying their high porosity also can somewhat generate physical adsorption for polysulfides. Proposed designs include microporous carbon,[16-18] mesoporous carbon,[6,19-22] core-shell structured carbon,[23] and functional carbon nanotubes (CNTs).[24-26] However, these scaffolds hardly provide adsorption strong enough to prevent diffusion of polysulfides in/out of their open structures. One exception exists when the pore size reaches micro-regime (< 0.6nm), when only short-chained sulfur species can be contained but not long-chained species.[16] The short-chained sulfur species are believed to be permanently trapped in the micro-pores during battery cycling. Regretfully, due to its unique pore structure, this design has severe limits on sulfur content in the composite, as well as output voltage and energy. Coating conductive polymer onto sulfur to form core-shell structures has also been explored to confine sulfur. The polymer shell seemed not dense enough to prevent polysulfide diffusion.[4-6,9,20,27,28] Finally, adsorption additives, mostly metal oxides with high surface areas, have low conductivity and will fundamental decrease battery capacity.[29-32]

Herein, we report nitrogen-doping in porous carbon scaffold to enhance its adsorption of sulfur species. The as-synthesized mesoporous nitrogen-doped carbon (MPNC) demonstrated much stronger adsorption of polysulfides. UV-visible spectroscopy study showed MPNC could

adsorb polysulfides over 5 times more than its nitrogen-free counterparts and other common adsorbents reported for Li-S batteries. Furthermore, MPNC also exhibited strong chemical bonding with sulfur. X-ray absorption technique (XANES) elucidated that this bonding was induced by N-doping, specifically nitrogen in pyridinic/pyrrolic-like positions. Applying this unique behavior of nitrogen-doped carbon in Li-S batteries, the MPNC-sulfur composite cathode showed excellent coulombic efficiency (>96%) and cycling stability (95% retention after 100 cycles). More importantly, high areal capacity (3.3 mAh/cm^2) can be demonstrated by using this novel cathode material, as the composite can be fabricated into electrodes with high sulfur loading (over 4 mg S/cm^2) while maintaining a good capacity of around 800 mAh/g.

4.2 Experimental Section

Synthesis of mesoporous nitrogen-doped carbon (MPNC): MPNC was synthesized by using commercial poly(melamine-co-formaldehyde) resin (84 wt. % solution in butanol) as the carbon precursor, with triblock copolymer Pluronic F127 ($PEO_{106}PPO_{70}PEO_{106}$), TEOS, and colloidal silica nanoparticles serving as poregens. The MF solution was diluted to 20 wt. % MF by addition of ethanol before use. Typically, 1.6 g Pluronic F127 was dissolved in a mixture of 15 ml of ethanol and 1.0 g of 0.2 M HCl under continuous stirring at 40 ^{o}C to form a homogeneous solution. Then 2.08 g TEOS, 5 ml of 20 wt. % colloidal silica latex, and 5.0 g of 20 wt. % MF solution were added in sequence. After being stirred for another 2 h, the final clear solution was transferred into petri dishes and the solvent was evaporated overnight in the fume hood at room temperature to produce transparent membranes. The membrane was further heated in an oven at 100°C for 12 h and then 150°C for 2 h to thermopolymerize the MF resin. Finally, the products were carbonized by heating them at 900°C for 2 h in argon, with a temperature ramping rate of 1°C/min, to obtain nitrogen-doped carbon-silica nanocomposites. Silica was removed by immersing the nanocomposites in 15 wt. % hydrofluoric acid solution for 24 h at room temperature, yielding a three dimensional hierarchical MPNC.

Synthesis of mesoporous carbon (MPC): Mesoporous carbon (MPC) is widely used as a conductive framework for sulfur cathodes. Herein, mesoporous carbon with similar surface area and pore volume to that of MPNC was selected as a control sample for our comparative study. The MPC was synthesized by an approach analogous to that used for MPNC by using phenolic resin as precursor according to publication by Zhao *et al.*.[22]

Preparation of lithium polysulfide in THF solution for UV-vis measurement: Typically, the stoichiometric amounts of sulfur (S) and lithium sulfide (Li_2S) with molar ratio of 5:1 were dissolved in tetrahydrofuran (THF) by magnetically stirring at room temperature for two days, yielding a deep red-orange solution. It should be noted that the whole synthesis procedure was carried out in an argon atmosphere.

Calculation of adsorption capacity: The adsorption capacity of carbon black (Super P), Al_2O_3, porous silica (SBA-15), mesoporous carbon (MPC), N-doped carbon (MPNC) in lithium polysulfide solution was investigated by UV-vis spectroscopy. Typically, 50 mg of one of the absorbents was placed in 20 ml of lithium polysulfide solution (0.25 mM) and the mixture was stirred for 10 min. The concentration of residual lithium polysulfides in the solution was determined by UV-Vis adsorption at 415 nm using Varian Cary 100 UV-visible spectrophotometer after the removal of adsorbents upon centrifugation. Based on the equilibrium plots, the residual concentration (C_r) of lithium polysulfide in the solution adsorption amount of lithium polysulfide was then determined, and then the adsorption capacity was calculated by taking the adsorption amount of lithium polysulfide onto unit mass of adsorbents as shown in the following equation:

$$Adsorption\ capacity\ (mg\ /\ g) = [(C_0 - C_r) \times V \times M] / m$$

Where, C_0 is the molar concentration of Li_2S_6 solution before adsorption; C_r is the molar concentration of Li_2S_6 solution after adsorption; V is the volume of the Li_2S_6 solution used in the adsorption test; M is the molar mass of Li_2S_6; m is the mass of adsorbent.

Characterization: The structure of the as-prepared composite was characterized by X-ray diffraction on a Rigaku Miniflex II spectrometer. X-ray photoelectron spectroscopy (XPS) measurements were carried out with a Kratos XSAM800 Ultra spectrometer. The surface

morphologies of the composite particles were investigated with a JEOL JSM-2010 transmission electron microscope (TEM). Elemental mapping was performed with a TEM operating in Electron Energy Loss Spectroscopy (EELS) mode. Elemental analysis was performed by on a CHMS-OEA 1108 elemental analyzer. The surface area and pore structure were characterized by nitrogen sorption using a Micrometrics ASAP 2020 physisorption analyzer. The surface area was calculated by the Brunauer–Emmett–Teller (BET) method. The pore size distributions (Dp) were derived from the adsorption branches of isotherms using the Barrett–Joyner–Halenda (BJH) model. The content of sulfur in the composites was characterized by thermogravimetric analysis (TGA) at a temperature range of 25-600°C with a heating rate of 10°C/min under nitrogen atmosphere.The C (284.2 eV), N (409.9 eV), and O (543.1 eV) K-edge X-ray absorption near edge spectroscopy (XANES) spectra were collected in partial electron yield mode at beamline U7A of the National Synchrotron Light Source (NSLS) at Brookhaven National Laboratory. Maximum 2wt.% of sulfur loading was applied to MPC and MPNC materials for XANES experiments due to the volatilization of sulfur species under ultra-high vacuum. The XANES spectra were processed and quantitatively analyzed using the ATHENA data analysis software via linear combination fitting.[33] Electrochemical impedance spectroscopy (EIS) measurement was performed using CHI 660D electrochemical workstation within the frequency range of 100 kHz to 10 mHz at potentiostatic signal amplitudes of 1mV.

Electrode film preparation and electrochemical tests: The composite cathode was prepared by mixing 80 wt. % composite powder, 10 wt. % Super P, and 10 wt. % polyvinylidene fluoride (PVDF) together in N-methyl-2-pyrrolidinone (NMP) to form a homogeneous slurry, then coating the slurry on aluminum foil and drying at 60°C for 10 h under vacuum. In this work, the sulfur mass loading in MPNC-S70 electrodes is typically as high as $4 - 5$ mg S/cm^2. (4.20 mg S/cm^2 for the electrode in Figure 5). Due to the higher polarization of MPNC-S80, MPC-S80, and

C-S80 electrodes, the sulfur mass loading of these electrodes was lower, around 1.1 mg/cm^2 (the

sulfur loading of MPNC-S80, MPC-S80 and C-S80 in Figure 4 are 1.11 mg/cm^2, 1.13 mg/cm^2,

and 1.05 mg/cm^2, respectively), in order to demonstrate the difference between the three

electrodes (i.e., nitrogen doping effects) without LiNO$_3$ additives. The electrochemical

performance of MPNC-S, MPC-S, and C-S was tested in a half-cell configuration using CR2016

type coin cells. The electrolyte was 1M LiTFSI dissolved in a mixture of 1,3-dioxolane (DOL)

and 1,2-dimethoxyethane (DME) (1:1 v/v), plus 0.2M LiNO$_3$ for 70 wt. % sulfur electrodes, and

the separator was a microporous polypropylene membrane (25 μm thick, Celgard 2400). Cells

were assembled in an argon-filled glove box and galvanostatically discharged and charged using

a battery tester (Arbin BT-2000) at room temperature.

4.3 Results and Discussion

4.3.1 Synthesis and characterization

The synthesis of MPNC involves evaporation-induced co-assembly of a polymer (as sources for both carbon and nitrogen) and porogens (to template meso-structure), followed by carbonization and removal of the porogens.[34,35] The selected polymer is a commercial resin, poly(melamine-co-formaldehyde), feasible for large scale fabrication. The initial mass ratio between nitrogen and carbon in the resin is 1:0.57, corresponding to its chemical formula $(C_4H_8N_6O)_n$. To get high pore volume for sulfur embedding as well as high surface area for polysulfide adsorption, a complex porogen system was adopted, consisting of tetraethyl orthosilicate (TEOS), amphiphilic triblock copolymers (Pluronic F127), silica colloids (ST-O, 10-20 nm in diameter) (see experimental section for details).

The porous structure of MPNC was analyzed by transmission electron microscopy (TEM) (**Figure 4-1a**) and nitrogen sorption measurement (**Figure 4-1b and c**). MPNC showed a disordered mesoporous structure, revealed by the TEM image. The pore-size distribution was quantitatively determined by applying the BJH (Barrett-Joyner-Halenda) model on the adsorption branch of the N_2 sorption isotherm. This distribution suggests a hierarchical pore structure of MPNC, composed of mesopores that peaks at 4nm in diameter (templated by hydrolyzed TEOS) and also those broadly distributed in a range of larger diameters (5-20nm, templated by both F127 and ST-O).[35] Also based on its nitrogen sorption isotherm, the Brunauer-Emmett-Teller (BET) surface area the BJH pore volume of MPNC were calculated to be 824.3 m^2/g and 1.38 cm^3/g,

respectively. The high pore volume and surface area designed for MPNC can afford high sulfur

content in the composite, as well as more active sites for polysulfide adsorption.
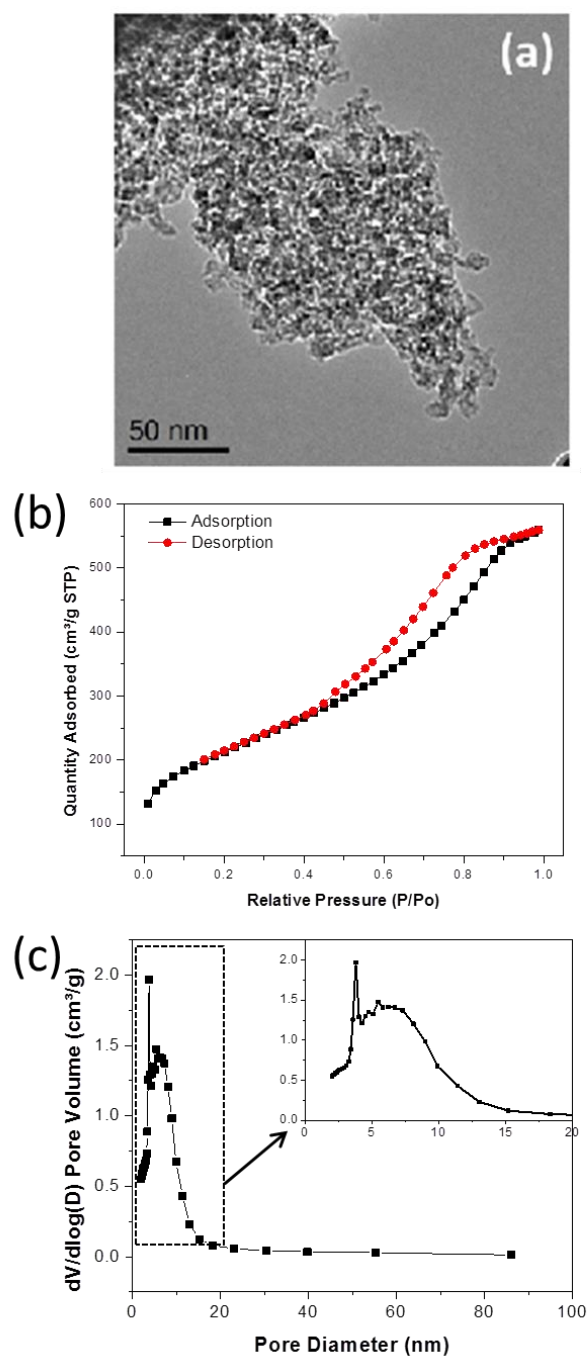
Figure 4-1. (a) TEM of MPNC; (b) N$_2$ sorption isotherms and (c) pore size distribution of MPNC.

Table 4-1. Results of the quantitative elemental analysis of MPC and MPNC

Samples	Elements (%)				
	C	N	H	O	other
MPC	91.19	-	1.50	6.23	1.08
MPNC	83.65	6.20	1.62	6.89	1.64
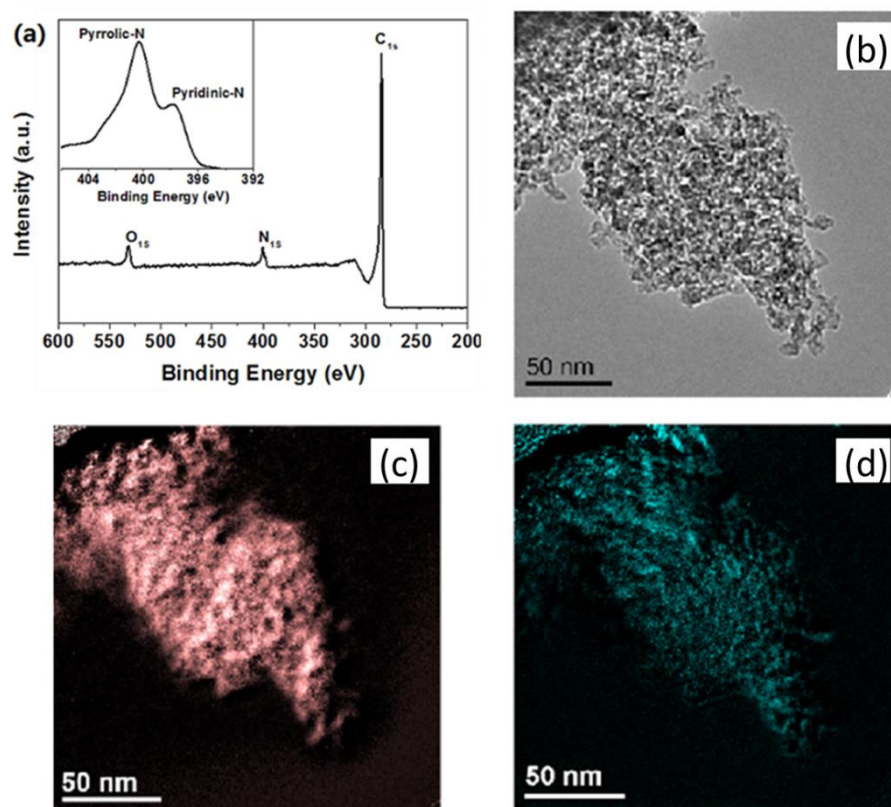
Figure 4-2. (a) Main: XPS survey spectrum of MPNC. Inset: High-resolution spectrum of the N 1s peak. The peaks at 397.8 eV and 400.3 eV correspond to pyridinic and pyrrolic N, respectively; (b) TEM image of an MPNC-S70 nanocomposite and corresponding EELS elemental maps of (c) carbon, (d) nitrogen.

The overall composition of the MPNC was investigated by elemental analysis (see Table 4-1). The ratio between nitrogen and carbon dropped to 1:13.5 after high-temperature carbonization (900°C). Nitrogen (6.20wt.%) and oxygen (6.89wt.%) are the two major dopants in

this carbon material with similar content. X-ray photoelectron spectroscopy (XPS) was performed

to probe the surface chemical composition of the MPNC (**Figure 4-2a**), showing the presence of

C, N, and O atoms in MPNC. The binding energy peaks observed in the high-resolution N 1s

profile at 397.8 eV and 400.3 eV (inset of **Figure 4-2a**) can be attributed to pyridinic and pyrrolic

nitrogen, respectively.[36-39] Although adsorption of polysulfide takes place on the carbon surface

and thus the nitrogen content on the surface is important, this value can't be accurately calculated

surface techniques such as XPS. However, its bulk content of 6.2% is a good indication as we

don't expect a large change in nitrogen content on the surface. Elemental mapping of carbon and

nitrogen showed uniform distribution on the MPNC sample (**Figure 4-2c and d**).

4.3.2 Polysulfides adsorption analysis by UV-vis measurement

To demonstrate the strong adsorption effect of nitrogen-doped carbon, the change in concentration of lithium polysulfide solution before and after exposure to MPNC, in comparison with other adsorbents, was measured by UV-Vis spectroscopy. The polysulfide solution used here has an overall stoichiometric ratio matching Li_2S_6 in THF solvent. Note that the chemical formula Li_2S_6 is only nominal as polysulfide compounds are known to disproportionate into different polysulfide species with different sulfur-chain length. Accordingly, several peaks located at 230 nm, 260 nm, and 415 nm were observed, shown in **Figure 4-3**. Among them, the absorbance peak at 415nm was found to be most stable and thus was selected for quantitative calculation for the adsorption capacity of different adsorbents in this study.[14] In the concentration range between 0.05mN and 1mN, the UV-vis absorbance at 415nm was found to have a strong linear relationship with the polysulfide concentration. The calibration curve was fitted to the linear equation: $Y=1.35X+0.0067$ ($R^2=0.9994$), where Y is the absorbance at 415nm and X is the concentration of polysulfide solution (**Figure 4-4**). The adsorption capacity of each adsorbent, calculated based on the calibration curve (see experimental section), was listed in **Table 4-2** together with their surface area and pore volume. A corresponding plot, **Figure 4-5**, provides a more visual comparison of the adsorption capacity among absorbents. Surface area apparently is critical for adsorption capacity as adsorption only occurs on the surface of each adsorbent. For example, the adsorption capacity of two carbon materials, Super P and MPC, are different, attributed to the large difference in surface area. More importantly, the surface property of the adsorbents also significantly affects the adsorption capacity. The surface property is largely determined by the chemical composition and structure of each adsorbent. Shown in **Table 4-2** and **Figure 4-5**, the adsorption capacity of MPNC is much higher than that of any other adsorbent in study. Even when compared with MPC, which boasts a higher surface area, MPNC out-

performed in adsorption by almost 6.5 times. The unusually strong adsorption ability of MPNC

should stem from the unique chemical structure involving nitrogen atoms on its surface.
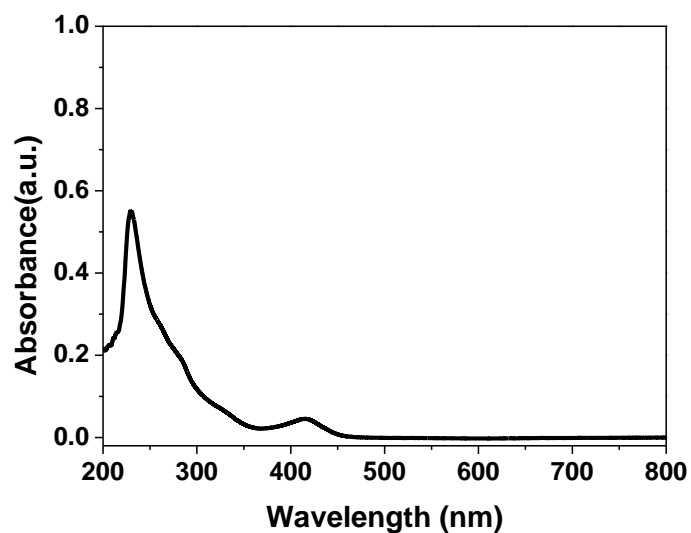
Figure 4-3. Typical UV-Vis absorption spectra of Li_2S_6 solution.
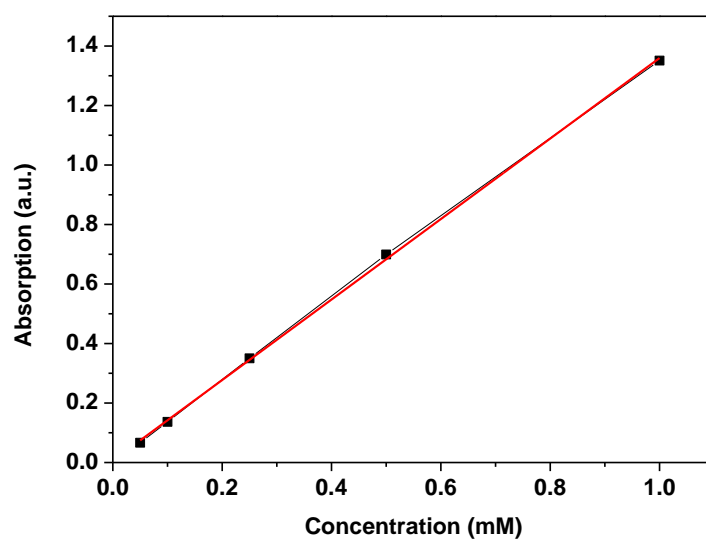
Figure 4-4. Calibration curve of the UV-Vis spectrometer with different concentration of lithium sulfide solution. A linear fit gives an equation of Y=1.35X+0.0067, R^2=0.9994.

Table 4-2. Summary of surface area, pore volume, and adsorption capacity of studied adsorbents

Sample	Surface area (m^2/g)	Pore Volume (cm^3/g)	Absorption $(g\ Li_2S_x/g)$
SBA-15	~850	~1.2	0.0123
Al_2O_3	98.0	0.24	0.0394
Super P	61.22	0.16	0.0123
Mesoporous carbon (MPC)	1014.0	2.5	0.0322
MPNC	824.3	1.38	0.2077
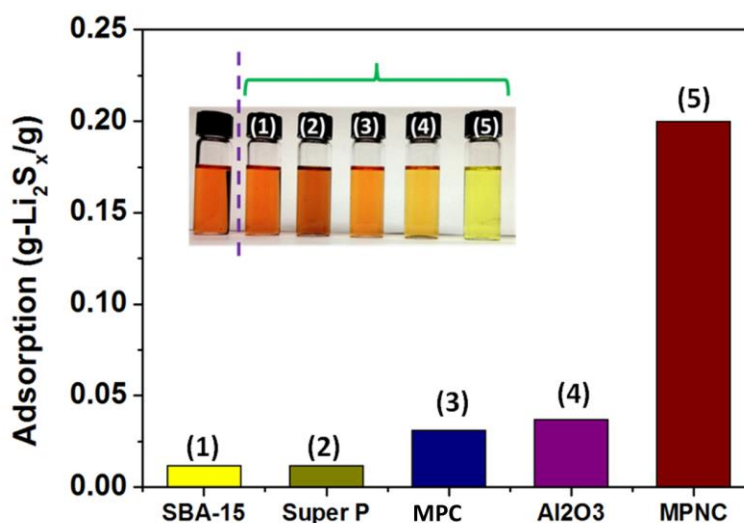
Figure 4-5. A comparison of the adsorption capacity of (5) MPNC and some traditional adsorbents, including (1) SBA-15, (2) Super P, (3) MPC, and (4) Al_2O_3. The insert is the photo image of polysulfide solution before and after exposure to different adsorbents.

4.3.3 X-ray adsorption analysis

We also studied the interaction between MPNC and sulfur using an X-ray absorption technique, X-ray Absorption Near Edge Structure or XANES. This interaction is also important to battery performance as it affects the re-deposition of sulfur when sulfur forms at the end of each charge process. XANES is very sensitive to local coordination structure around a specific element of interest. We studied the XANES spectra of four samples, MPNC, MPNC-S2, MPC, and MPC-S2. MPNC-S2 is a composite containing 2wt.% sulfur and 98wt.% MPNC. It was formed by grind-mixing MPNC and sulfur and kept at 155 °C for 10 hours. Under such temperature, sulfur is in liquid phase and would diffuse into the pores of MPNC due to capillary force. We chose to control its sulfur content at a low level of 2wt.% in order to guarantee the formation of only thin coating of sulfur on the pore walls of MPNC without any aggregation of sulfur, thus to avoid undesirable interference in the XANES spectrum. MPC-S2 was formed the same way using MPC and sulfur. No pronounced peak shift was observed in the C or N spectrum of MPNC after forming sulfur composite, indicating no change in coordination structures (**Figure 4-6**). However, there is a significant change in O coordination structure of MPNC after introducing the thin coating of sulfur (**Figure 4-7**). Oxygen presents in relatively more ether-type functional groups and relatively less carboxyl-type and/or carbonyl-type functional groups in MPNC-S (after sulfur embedding) than in MPNC (before sulfur embedding), indicated by data fitting based on reference compounds (**Table 4-3**).[40] This change in the local coordination structure of oxygen indicates that oxygen in carbonyl and carboxyl groups of MPNC may have bonded to sulfur. On the other hand, although oxygen also exists in MPC, no peak shift was observed after sulfur embedding in the oxygen XANES spectrum (**Figure 4-7**). Neither was in its carbon XANES spectrum (**Figure 4-6**). The independence of peak position with sulfur

embedding in these spectra indicates that there is no significant chemical interaction between

MPC and sulfur.
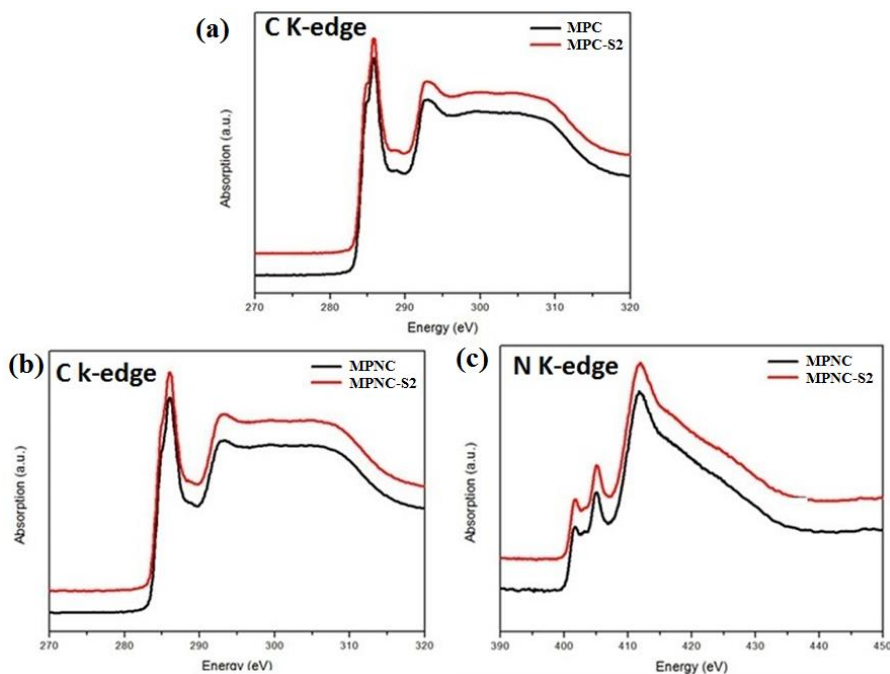
Figure 4-6. (a) Carbon K-edge XANES spectra of MPC and MPC-S2 and (b) MPNC and MPNC-S2; (c) Nitrogen K-edge XANES spectra of MPNC and MPNC-S2. (This characterization work was conducted by Pengyu Zhu at Brookhaven National Lab.)
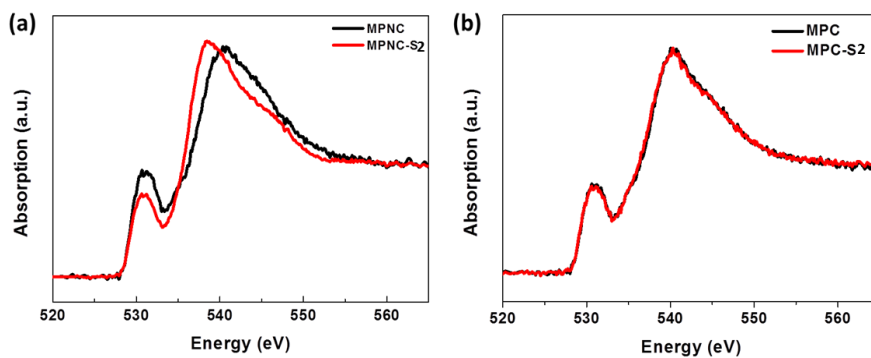
Figure 4-7. (a) Oxygen K-edge XANES spectra of MPNC and MPNC-S2 nanocomposites; (b) Oxygen K-edge XANES spectra of MPC and MPC-S2 nanocomposites. (This characterization work was conducted by Pengyu Zhu at Brookhaven National Lab.)

Table 4-3. Linear combination fitting of oxygen functional groups of MPNC and MPNC-S2

Sample	Carbonyl	Carboxyl	Hydroxyl/Ether
MPNC	16.0%	54.9%	31.4%
MPNC-S2	8.6%	38.7%	48.6%

(Note: The oxygen functional groups on MPNC material before and after forming sulfur embedding were determined via linear combination fitting of XANES spectra for those materials using reference spectra. All reference spectra were collected in partial electron yield mode at beamline U7A at NSLS. Two representative reference compounds were chosen for each type of functional group, namely the carbonyl group (polyvinylpyrrolidone and poly(vinyl methyl ketone)), carboxyl group (poly(ethylene-alt-maleic anhydride) and poly(acrylic acid)), and hydroxyl group (polyvinyl alcohol and poly(4-vinylphenol)). Fitting was done using the ATHENA data analysis software. It is important to note that ether group XANES spectra have similar shapes to hydroxyl group spectra, making the two very difficult to distinguish. Therefore, ether and hydroxyl spectra were fit together and only the net fraction of these groups in the materials is presented here. The fitting results indicate a decrease of carboxyl groups and an increase of hydroxyl/ether groups after embedding sulfur at 155°C. Please note that the sum of abundance was not forced to be 1 when performing the fitting, whereas a convergence at 1 is expected for a good fitting result.)

4.3.4 Battery performance of MPNC-S composite

The MPNC-sulfur nano-composites were prepared by a melt-diffusion method. Typically, sulfur and MPNC were grind-mixed and then heated at 155°C for 10 h, causing the molten sulfur to flow into the pores of the MPNC by capillary force. The resultant composite is denoted as MPNC-SX, where X is the weight percentage of sulfur in the composite. Two samples, MPNC-S70 and MPNC-S80, were tested as the cathode materials for Li-S batteries. The sulfur content in these two composites was confirmed by thermogravimetric analysis (TGA, **Figure 4-8a**). X-ray diffraction measurement showed no peaks on the MPNC-S70 composite, indicating amorphous state of sulfur in this composite (**Figure 4-8b**). In contrast, MPNC-S80 composite showed mild XRD peaks, indicating the formation of sulfur crystallites (**Figure 4-8c**). The sulfur crystallites should be the excessive part of sulfur not contained in the pores but growing on the periphery of carbon particles. The two corresponding control samples of MPC composites with the same sulfur content, MPC-S70 and MPC-S80, showed similar results of XRD measurement because of similar porosity.
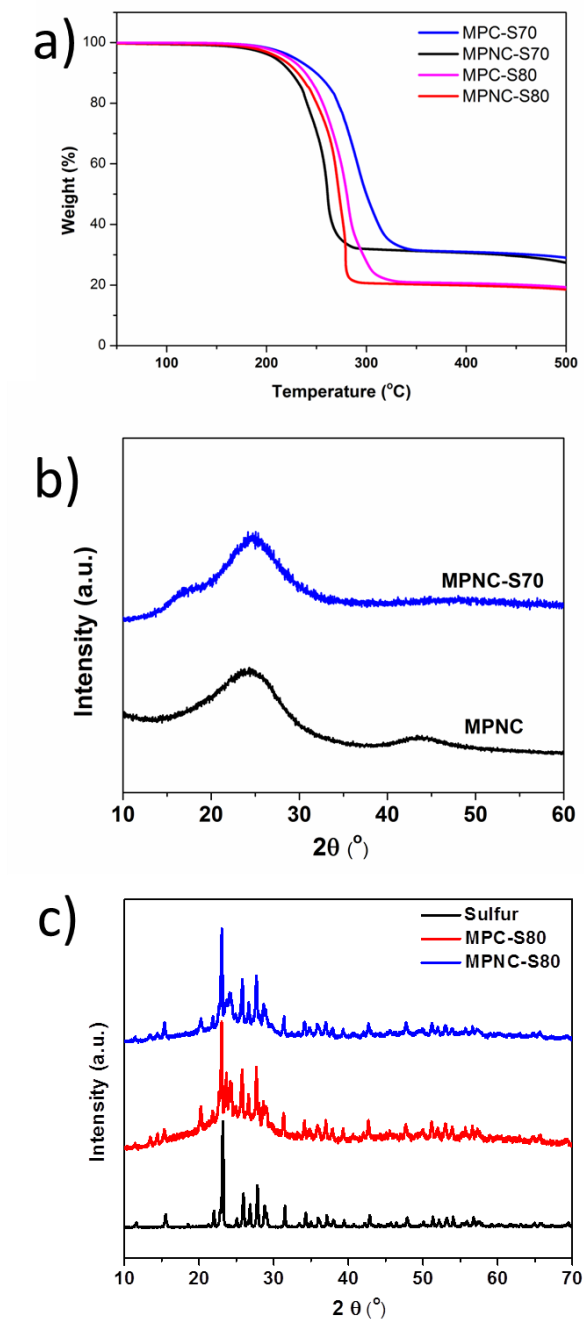
Figure 4-8. (a) TGA curves of composites with a heating rate of 10°C/min under nitrogen atmosphere; (b) XRD pattern of MPNC-S70; (c) XRD patterns of MPNC-S80 and MPC-S80.

MPNC-sulfur composites were evaluated as cathode materials of Li-S batteries in order to see if the exceptional adsorption of polysulfides on MPNC had favorable effects on battery performance. The as-synthesized MPNC, together with two other nitrogen-free carbon samples (MPC and Super P) as controls, were used to form sulfur composites and tested as Li-S cathode materials. The typical sulfur loading of these electrodes is ~1.1 mg S/cm^2 and the battery performance was studied in two-electrode CR2016 coin cells using a galvanostatic charge-discharge process with 1M lithium bis(trifluoromethanesulfonyl)imide (LiTFSI) in 1,3-dioxolane/dimethoxy ethane (DOL/DME, 1:1 volumetric ratio) as the electrolyte. **Figure 4-9a** shows typical discharge-charge voltage profiles of MPNC-S80, MPC-S80, and C-S80 (Super P-sulfur mixture) cathodes at a current rate of C/10 (0.168 mA/g) between 1.5V and 3.0V. The voltage profiles show distinct differences between MPNC-S80 and the control cathodes. Significant polarization was observed in the charge/discharge profiles of both MPC-S80 and C-S80 due to decreased conductivity of the cathodes. In contrast, MPNC-S80 still clearly shows discharge plateaus of 2.3 V and 2.1 V, indicating much less polarization at such high sulfur content. The lower resistance and polarization observed on the MPNC-S80 sample should be attributed to a more ideal distribution of sulfur in the composite, compared with MPC-S80 sample in particular. Although 80wt.% sulfur content exceeded the pore capacity in both samples via the capillary embedding process (as indicated by XRD patterns), the strong interaction between MPNC and sulfur may have still resulted in a more even distribution of sulfur and a more intimate contact between the two. The initial discharge capacity of MPNC-S80 was 1013 mAh g^{-1} as shown in **Figure 4-9c**. At the second cycle, a large reversible capacity of about 1008 mAh g^{-1} is obtained, corresponding to capacity retention of ~99.5%, which is much higher than that of MPC-S80 (~86.6%) and C-S80 (~91.1%). Over the testing span of 50 cycles at 0.17 mAh/cm^2, MPNC-S80 exhibited noticeably higher reversible capacity than MPC-S80 and C-S80. The higher utilization rate suggests less diffusion loss of sulfur species in the electrolyte. Furthermore,

polysulfides are known to undergo shuttle effect and suppress the coulombic efficiency at a low level. The fact that the coulombic efficiency is significantly higher when using MPNC-sulfur composite also suggests less polysulfides diffusing in the electrolyte. Both higher capacity and coulombic efficiency for the MPNC-S80 sample can good indications that polysulfides are better confined in the cathode, due to nitrogen-doping-induced chemical adsorption by MPNC. The chemical adsorption can facilitate uniform dispersion of sulfur during sulfur loading and uniform redeposition of sulfur at the end of delithiation (charge process), thus decreasing charge transfer resistance and mitigating diffusion loss of polysulfides away from the cathode. This is believed to be because the sulfur bonded to oxygen functional groups of the MPNC can easily bond to open sulfur atoms of sulfur chains, such as partly-delithiated polysulfides (i.e., LiS_x^-)[41,42] or S_x chains formed upon heating during sulfur loading.[16,43] This would allow the formation of sulfur chains bonded to the surface at the oxygen functional groups, which should be evenly distributed across the carbon surface, rather than allowing polysulfides to fully delithiate to free S_8 molecules and aggregate into large particles at the surface.
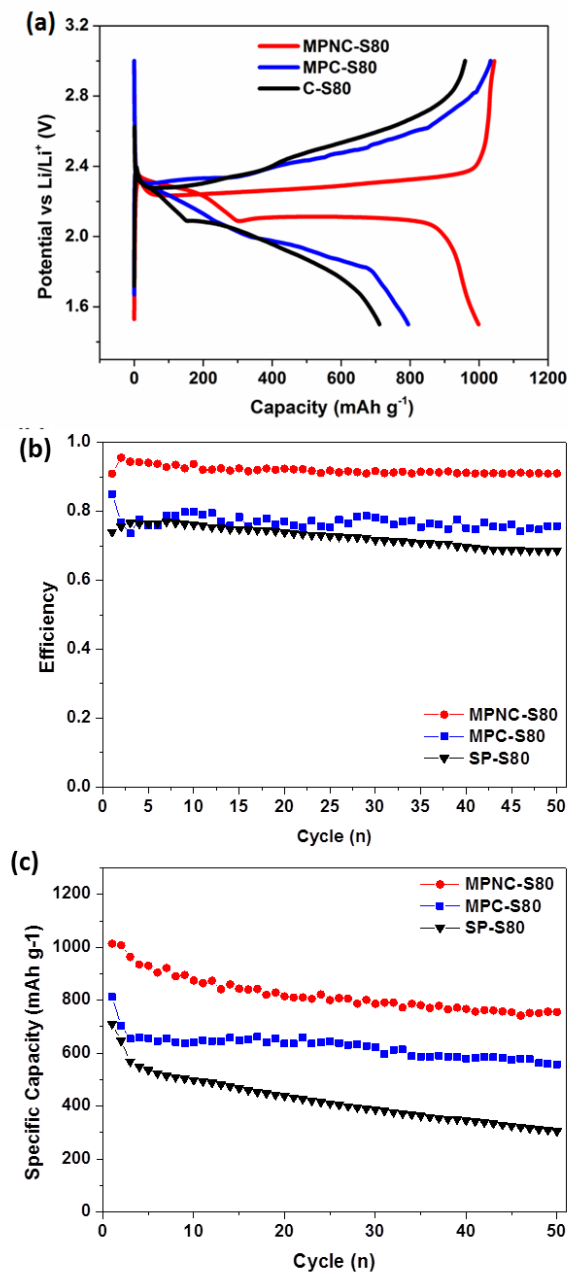
Figure 4-9. (a) Initial discharge–charge voltage-capacity profiles three composites containing 80wt.% sulfur; (b) cycling performance and (c) coulombic efficiency of three composites at a current density of 0.18 mA/cm^2. Split capacity and CE.

In order to demonstrate the potential of the MPNC-S composite cathode for practical use, MPNC-S70 (70 wt.% S) cathodes with a high loading of 4.2 mg-S/cm^2 were fabricated. The sulfur content was slightly decreased in this setting (from 80 wt.% to 70 wt.%) to ensure that sulfur was contained within the pores of the carbon framework and thus grant the electrode a higher conductivity. For electrochemical testing of these electrodes, lithium nitrate (LiNO$_3$, 0.2M in electrolyte) was used as an electrolyte additive to further improve the coulombic efficiency, as LiNO$_3$ can protect Li anode from reacting with soluble polysulfides.[44,45] **Figure 4-10a** shows a typical discharge-charge profile of an MPNC-S70 cathode at a current density of 0.35 mA/cm^2 between 1.7V and 3.0V. The discharge curve shows two plateaus at 2.3 V and 2.1 V vs. Li/Li$^+$, corresponding to the reduction of sulfur to higher order lithium polysulfides (Li$_2$S$_n$, 6≤n≤8) and the reduction of higher-order lithium polysulfides to lower-order lithium polysulfides (Li$_2$S$_n$, 2≤n<6) and Li$_2$S, respectively.[6,46] The reverse reactions, corresponding to the oxidation of low order polysulfides and high order polysulfides, were displayed in the charge curve with two potential plateaus around 2.2 V and 2.4 V, respectively.[18] The cycle life and coulombic efficiency of the MPNC-S70 nanocomposite cathode are shown in **Figure 4-10b**. MPNC-S70 delivers an initial specific capacity of 1100 mAh/g and coulombic efficiency of 99.4% at a current density of 0.35 mA/cm^2. The second cycle delivers a high reversible capacity of 990 mAh/g. After the first two activation cycles at 0.35 mA/cm^2, the cell was switched to 0.70 mA/cm^2 for another 100 cycles. The capacity quickly stabilized at ~800 mAh/g and showed roughly 95 % retention after 100 cycles at a current density of 0.70 mA/cm^2. That means only 0.05% capacity loss per cycle, which is outstanding compared with previous reports. The high coulombic efficiency (96~99%) of the MPNC-S70 nanocomposite is probably due to synergetic effects of both the LiNO$_3$ additive and nitrogen-doping-induced chemical adsorption.

The areal capacity of MPNC-S electrodes is calculated as specific capacity (mAh/g) of sulfur $\times$ sulfur mass loading (g sulfur/cm^2 of electrode face area). Based on this, it is clear that achieving a high areal capacity necessitates high sulfur loading in the electrodes. Most of the high specific capacities reported in the literature for electrodes fabricated by coating techniques were obtained at a low sulfur loading (below 2 mg S/cm^2) and/or low sulfur content (below 70 wt.%). [6,8,16,19,47,48] This loading is insufficient to achieve a cathode with energy density greater than that of present Li-ion cathodes, as previously described. For this work, the MPNC-S cathode with a sulfur loading of 4.2 mg S/cm^2 and high sulfur content of 70 wt.% can deliver an areal capacity of 3.3 mAh/cm^2 (**Figure 4-10c**), which is 2-10 times higher than other reports.[6,8,16,19,47,48] The areal capacity values estimated from recent publications are shown in the Li-S cell specific energy plot for comparison purposes.
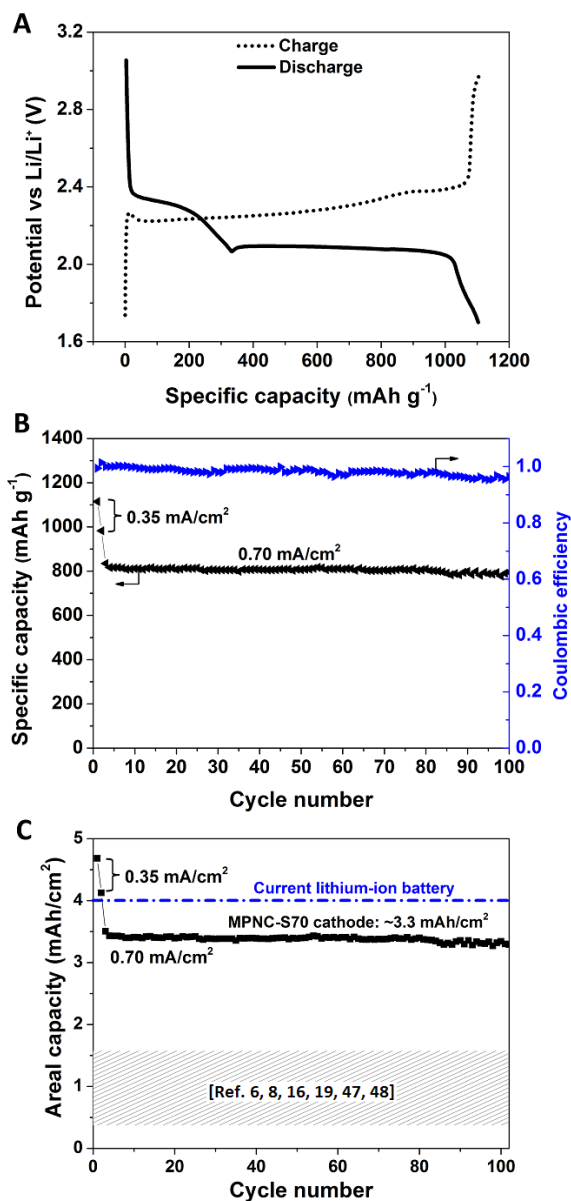
Figure 4-20. (a) A typical first cycle discharge-charge voltage-capacity profile of an MPNC-S70 nanocomposite cathode at a current density of 0.35 mA/cm²; (b) Cycle performance and coulombic efficiency of MPNC-S70 cycled at a current density of 0.35 mA/cm² for the first two cycles and 0.70 mA/cm² for the subsequent cycles. The capacity values were calculated based on the mass of sulfur; (c) The areal capacity of MPNC-S70 cathode with a sulfur loading of 4.2 mg S/cm² and sulfur content of 70 wt.%. The areal capacity is calculated by specific capacity (mAh/g) × sulfur loading (mg S/cm²). The areal capacity of current lithium-ion battery is around 2-4 mAh/cm². The MPNC-S70 cathode shows an areal capacity of ~3.3 mAh/cm², which is close to the high-end value of lithium-ion batteries. Areal capacity ranges of reported sulfur cathodes in references are also marked in grey.

4.4 Conclusion

In summary, we have developed a novel, mesoporous, nitrogen-doped carbon (MPNC)-sulfur nanocomposite as a cathode for Li-S batteries. The nitrogen doping in the MPNC material was found to promote formation of bonds between sulfur atoms and oxygen functional groups on the carbon, which is believed to play a key role in sulfur immobilization. This S-O chemical bonding was directly observed by XANES. Based on the advantages of their structure and composition, the MPNC-S cathodes show excellent cycling stability at high current density of 0.7 mAh/cm^2 with a high sulfur loading (4.2 mg S/cm^2) and sulfur content (70 wt.%). The areal capacity of MPNC-S70 cathodes can reach ~3.3 mAh/cm^2, which is superior to other reports. This novel nitrogen-doped carbon, as well as the related chemical adsorption mechanism, is very helpful for developing novel cathodes for lithium-sulfur batteries.

Reference (Chapter 4)

1   Bruce, P. G., Freunberger, S. A., Hardwick, L. J. & Tarascon, J. M. *Nat. Mater.* **2012**, 11, 19-29.

2   Wang, D. *et al. J. Mater. Chem. A* **2013**, 9382-9394.

3   Ji, X. & Nazar, L. F. *Journal of Materials Chemistry* **2010**, 20, 9821-9826.

4   Schuster, J. *et al. Angewandte Chemie International Edition* **2012**, 51, 3591-3595.

5   Jayaprakash, N., Shen, J., Moganty, S. S., Corona, A. & Archer, L. A. *Angewandte Chemie International Edition* **2011**, 50, 5904-5908.

6   Ji, X., Lee, K. T. & Nazar, L. F. *Nat. Mater.* **2009**, 8, 500-506.

7   Manthiram, A., Fu, Y. & Su, Y. S. *Acc. Chem. Res.* **2012,** 46, 1145.

8   Ji, X., Evers, S., Black, R. & Nazar, L. F. *Nat. Commun.* **2011**, 2, 325.

9   Xiao, L. *et al. Adv. Mater.* **2012**, 24, 1176-1181.

10   Ji, L. *et al. J. Am. Chem. Soc.* **2011**, 133, 18522-18525.

11   Hayashi, A., Ohtomo, T., Mizuno, F., Tadanaga, K. & Tatsumisago, M. *Electrochem. Commun.* **2003**, 5, 701-705.

12   Nelson, J. *et al. J. Am. Chem. Soc.* **2012**, 134, 6337-6343.

13   Demir-Cakan, R. *et al. Energy. Environ. Sci.* **2013,** *6,* 176.

14   Barchasz, C. *et al. Analytical Chemistry* **2012**, 84, 3973-3980.

15   Cheon, S. E. *et al. J. Electrochem. Soc.* **2003**, 150, A800-A805.

16   Xin, S. *et al. Journal of the American Chemical Society* **2012**, 134, 18510-18513.

17   Zhang, B., Qin, X., Li, G. & Gao, X. *Energy. Environ. Sci.* **2010**, 3, 1531-1537.

18   Su, Y.-S. & Manthiram, A. *Nat. Commun.* **2012**, 3, 1166.

19   Schuster, J. *et al. Angewandte Chemie International Edition* **2012**, 51, 3591-3595.

20   Liang, C., Dudney, N. J. & Howe, J. Y. *Chemistry of Materials* **2009**, 21, 4724-4730.

21   He, G., Ji, X. & Nazar, L. *Energy. Environ. Sci.* **2011**, 4, 2878-2883.

22   Chen, S. R. *et al. Electrochim. Acta* **2011**, 56, 9549-9555.

23   Zhang, C., Wu, H. B., Yuan, C., Guo, Z. & Lou, X. W. *Angew. Chem. Int. Ed* **2012**, 51, 9592-9595.

24   Dorfler, S. *et al. Chem. Commun.* **2012**, 48, 4097-4099.

25   Guo, J., Xu, Y. & Wang, C. *Nano Letters* **2011**, 11, 4288-4294.

26   Chen, J. J. *et al. Phys. Chem. Chem. Phys.* **2012**, 14, 5376-5382.

27   Yang, Y. *et al. ACS Nano* **2011**, 5, 9187-9193.

28   Kim, J. *et al. Adv. Funct. Mater.* **2013**, 23, 1076-1080.

29   Ji, X., Evers, S., Black, R. & Nazar, L. F. *Nat Commun* **2011**, 2, 325.

30   Zhang, Y. *et al. Solid State Ionics* **2010**, 181, 835-838.

31   Choi, Y. J. *et al. Physica Scripta* **2007**, T129, 62-65.

32   Evers, S., Yim, T. & Nazar, L. F. *The Journal of Physical Chemistry C* **2012**, 116, 19653-19658.

33   Ravel, B. & Newville, M. *Journal of Synchrotron Radiation* **2005**, 12, 537-541.

34   Deng, Y. *et al. J. Am. Chem. Soc.* **2007**, 129, 1690-1697.

35   Liu, R. *et al. Journal of the American Chemical Society* **2006**, 128, 11652-11662.

36   Wang, H., Maiyalagan, T. & Wang, X. *ACS Catalysis* **2012**, 2, 781-794.

37   Qie, L. *et al. Adv. Mater.* **2012**, 24, 2047-2050.

38   Shin, W. H., Jeong, H. M., Kim, B. G., Kang, J. K. & Choi, J. W. *Nano Lett.* **2012**, 12, 2283-2288.

39   Sun, L. *et al. RSC Advances* **2012**, 2, 4498-4506.

40   Kim, K., Zhu, P., Li, N., Ma, X. & Chen, Y. *Carbon* **2011**, 49, 1745-1751.

41   Lin, Z., Liu, Z., Fu, W., Dudney, N. J. & Liang, C. *Angewandte Chemie International Edition* **2013**, 52, 7460-7463.

42   Wang, J. *et al. Adv. Funct. Mater.* **2003**, 13, 487-492.

43   Meyer, B. *Chem. Rev.* **1976**, 76, 367-388.

44   Aurbach, D. *et al. J. Electrochem. Soc.* **2009**, 156, A694.

45   Zhang, S. S. *Electrochim. Acta* **2012**, 70, 344-348.

46   Yuan, L. X. *et al. Electrochemistry Communications* **2006**, 8, 610-614.

47   Lee, Y. M., Choi, N. S., Park, J. H. & Park, J.-K. *J. Power Sources* **2003**, 119–121, 964-972.

48   Zhao, S. *et al. Journal of Materials Chemistry A* **2013**, 1, 3334-3339.

Chapter 5

Conclusions

This dissertation work focused on the study of material chemistry and engineering for lithium-sulfur batteries. In particular, several novel porous carbon-sulfur composites were proposed as the cathode materials for lithium-sulfur batteries.

The work in Chapter 2 focused on tuning the nanostructure of porous carbon-sulfur composite in order to improve electrochemical performance of the C-S composite cathode material. A tri-constituent pore system in evaporation-induced self-assembly (EISA) process was adopted to synthesize the porous carbon, HPC, as sulfur host with large pore volume (3.2 cm^3/g) and large surface area (1629 m^2/g). At the same time, its pores were restrained under 20nm. Such a nanostructure of the porous carbon has several favorable properties to form sulfur composite as a Li-S cathode material. The large pore volume of small pores can contain a high percentage of sulfur in nanoscale. In addition, the large surface area not only provide active reaction site, but also exert physical adsorption on polysulfides to mitigate capacity decay of such batteries. HPC-S80 composite demonsrated exceptional battery performance with a high sulfur content of 80wt.%, which leads to a high energy density of the overall composite and a low cost.

The work in Chapter 3 focused on forming secondary structure of C-S composite in order to improve its energy density (both gravimetric and volumetric). Several parameters other than the sulfur-specific capacity and coulombic efficiency are critical for the development of high energy lithium-sulfur batteries, including tap density of the cathode, sulfur content in the cathode, and sulfur loading on the cathode. We modified the synthesis of porous carbon described in chapter 2 to an emulsion polymerization setting in order to control simultaneously nanostructure

and micro-sized particle morphology. This synthesis protocol resulted in porous carbon microspheres, PSC, with a highly porous nanostructure and a desirable particle-size distribution in micro scales for battery applications. The resultant C-S composite showed enhanced battery performance on various aspects, including tap density, areal capacity, and projected gravimetric and volumetric energy density of the whole battery. What's more, carbon nanotubes can be well dispersed in the microspheres during the synthesis stage, boosting the battery performing of the composite at higher current densities. The proposed synthesis method is also highly scalable and versatile to incorporate extra building blocks into the C-S composite.

The work in chapter 4 focused on functionalizing porous carbon to stabilize battery performance. Lithium-sulfur batteries severely suffer from performance decay because sulfur has diffusion loss in forms of lithium polysulfides. It was observed that nitrogen doping in carbon could significantly enhance carbon's adsorption of polysulfides, consequently mitigate the diffusion loss of polysulfides and performance decay. This work details the synthesis and characterization of nitrogen-doped porous carbon, the study of its enhanced interaction with sulfur and polysulfides, and improved battery performance from its sulfur composite.

VITA

Tianren Xu

Tianren Xu was born in Jiaxing, Zhejiang province, on the east coast of China, on July 18th, 1985. He attended Fudan University in Shanghai where he obtained his Bachelor of Science degree in Aerospace Engineering in June 2009. Tianren began his graduate studies at The Pennsylvania State University under the guidance of Assistant Professor Donghai Wang in January of 2010.